

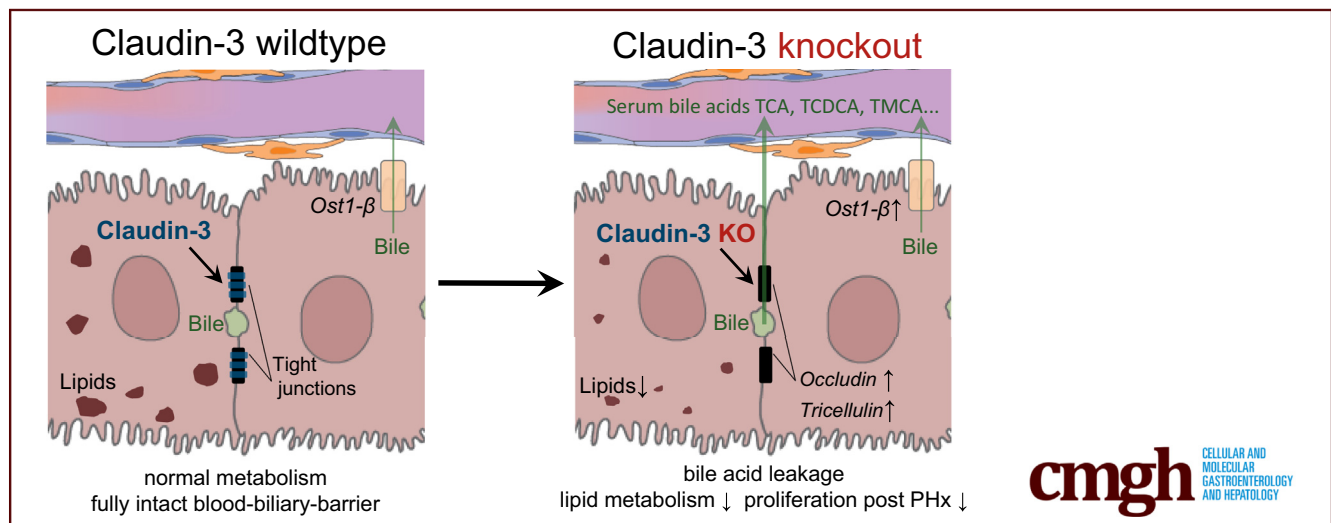
ORIGINAL RESEARCH

Loss of Claudin-3 Impairs Hepatic Metabolism, Biliary Barrier Function, and Cell Proliferation in the Murine Liver



Felix Alexander Baier,¹ Daniel Sánchez-Taltavull,¹ Tural Yarahmadov,¹ Cristina Gómez Castellà,² Fadi Jebbawi,² Adrian Keogh,¹ Riccardo Tombolini,¹ Adolfo Odriozola,³ Mariana Castro Dias,⁴ Urban Deutsch,⁴ Mikio Furuse,⁵ Britta Engelhardt,⁴ Benoît Zuber,³ Alex Odermatt,² Daniel Candinas,¹ and Deborah Stroka¹

¹Visceral Surgery and Medicine, Inselspital, Bern University Hospital, Department for BioMedical Research, ³Institute of Anatomy, ⁴Theodor Kocher Institute, University of Bern, Bern, Switzerland; ²Division of Molecular and Systems Toxicology, Department of Pharmaceutical Sciences, University of Basel, Basel, Switzerland; ⁵Division of Cell Structure, National Institute for Physiological Sciences, Okazaki, Japan



SUMMARY

Delineating the cell type-specific expression of hepatic tight junction genes showed that claudin-3 is the predominant tight junction protein on hepatocytes and cholangiocytes. In vivo study of claudin-3 knockout mice showed that claudin-3 is necessary to maintain lipid metabolism, biliary-barrier function, and optimal liver regeneration.

BACKGROUND & AIMS: Tight junctions in the liver are essential to maintain the blood-biliary barrier, however, the functional contribution of individual tight junction proteins to barrier and metabolic homeostasis remains largely unexplored. Here, we describe the cell type-specific expression of tight junction genes in the murine liver, and explore the regulation and functional importance of the transmembrane protein claudin-3 in liver metabolism, barrier function, and cell proliferation.

METHODS: The cell type-specific expression of hepatic tight junction genes is described using our mouse liver single-cell sequencing data set. Differential gene expression in *Cldn3*^{-/-} and *Cldn3*^{+/+} livers was assessed in young and aged mice by RNA sequencing (RNA-seq), and hepatic tissue was analyzed for

lipid content and bile acid composition. A surgical model of partial hepatectomy was used to induce liver cell proliferation.

RESULTS: Claudin-3 is a highly expressed tight junction protein found in the liver and is expressed predominantly in hepatocytes and cholangiocytes. The histology of *Cldn3*^{-/-} livers showed no overt phenotype, and the canalicular tight junctions appeared intact. Nevertheless, by RNA-seq we detected a down-regulation of metabolic pathways in the livers of *Cldn3*^{-/-} young and aged mice, as well as a decrease in lipid content and a weakened biliary barrier for primary bile acids, such as taurocholic acid, taurochenodeoxycholic acid, and taurine-conjugated muricholic acid. Coinciding with defects in the biliary barrier and lower lipid metabolism, there was a diminished hepatocyte proliferative response in *Cldn3*^{-/-} mice after partial hepatectomy.

CONCLUSIONS: Our data show that, in the liver, claudin-3 is necessary to maintain metabolic homeostasis, retention of bile acids, and optimal hepatocyte proliferation during liver regeneration. The RNA-seq data set can be accessed at: <https://www.ncbi.nlm.nih.gov/geo/query/acc.cgi?acc=GSE159914>. (*Cell Mol Gastroenterol Hepatol* 2021;12:745-767; <https://doi.org/10.1016/j.jcmgh.2021.04.003>)

Keywords: Tight Junction; Bile Acid; Liver Regeneration; Claudin; Single-Cell RNA Sequencing.

Tight junction (TJ) proteins can be found in almost every organ of the body, where their primary function is to create a semipermeable paracellular barrier that restricts passage of ions and solutes.¹ TJ protein expression is highly organ-specific.^{2,3} In the liver, TJs act as a separator of bile and blood circulation in hepatocytes and cholangiocytes.⁴ The molecular components of hepatic TJs comprise a number of different transmembrane and cytoplasmic proteins that have varying expression intensity and localization within the tissue.⁴ Thus far, the cell type-specific expression of hepatic TJ proteins has remained largely unexplored.

The protein family that best defines the barrier and sealing properties of a TJ are the claudins.⁵ Claudins are transmembrane proteins that have 27 known family members in human beings.⁶ Structurally, claudins consist of 4 transmembrane segments, 2 extracellular loops, and 1 intracellular loop, with the N-terminus and C-terminus facing the cytosol. The C-terminal end also harbors the Post synaptic density95/SAP90- Drosophila disc large tumor suppressor- Zonula occludens-1 (PDZ)-binding motif, which is the binding site for other proteins of the TJ complex.⁷⁻⁹ The extracellular loops of some claudins may serve as binding sites for hepatitis C virus or *Clostridium perfringens* enterotoxin.¹⁰⁻¹³ Sealing-type claudin-1, -3, -5, -11, -14, and -19 form a tightly closed paracellular barrier, whereas the pore-forming claudin-2, -10a/b, -15, -17, and -21 enable the selective passage of ions and solutes.^{6,14,15} Previous reports have shown that claudins of both sealing and pore-forming types can be found in liver tissue.⁴ Mutations and/or abnormal expression of claudin proteins is associated with multiple hepatic morbidities such as hepatomegaly, jaundice, portal hypertension, restricted bile flow, or cirrhosis.¹⁶⁻¹⁹ For example, absence of sealing claudin-1 may cause the rare genetic disease neonatal ichthyosis and sclerosing cholangitis, in which patients present with cholestasis and increased serum levels of γ -glutamyltransferase, transaminase activity, and bilirubin.^{16,17} Knockout of pore-forming claudin-2 on the other hand reduces bile flow and concentrates lipids and acids within the hepatic bile of mice.¹⁸ Claudin-3 is another sealing-type claudin^{20,21} that controls the barrier for calcium phosphate ions.²² Intestinal studies have shown that claudin-3 expression changes in high-fat or inflammatory environments, suggesting a role for metabolic regulation.²³⁻²⁵ Until now, it was not known if claudin-3 contributed to liver lipid metabolism or regenerative recovery after tissue loss.

Using data from single-cell RNA sequencing, we delineate the cell type-specific TJ gene expression of a mouse liver. We identified *Cldn3* as one of the most abundant transmembrane TJ genes in the liver with expression in hepatocytes and cholangiocytes. Using *Cldn3*^{-/-} mice, we found that claudin-3 is essential for the liver's metabolic homeostasis and that loss of claudin-3 impairs hepatocyte proliferation after partial hepatectomy (PHx).

Results

Expression Profile of TJ Genes in Hepatic Cells


To describe the hepatic expression of TJ genes, we used our recently published single-cell RNA sequencing (scRNA-

seq) data set of parenchymal and nonparenchymal cells from a C57BL/6 liver.²⁶ Unsupervised clustering identified 14 unique cell clusters (Figure 1A). A defined set of marker genes and clustering for cell classification identified the populations of hepatocytes, cholangiocytes, endothelial cells, immune cells, and stellate cells (Figure 1B). Expression of TJ genes within these 5 populations is shown in the heatmap, with hepatocytes expressing *Cldn3*, *Cldn5*, *Cldn12*, *Jam-a*, and *Pard3*. Cholangiocytes expressed high levels of *Cldn3*, *Cldn6*, *Cldn7*, and *Jam-a*. Endothelial and stellate cells expressed mostly *Cldn5*, but also *Jam-a*, *Jam-b*, and others. TJ messenger RNA (mRNA) also could be detected in immune cells, including *Cldn5*, *Jam-a*, *Sympk*, and *Ybx3* (Figure 1C). Some TJ genes, such as *Jam-a* and *Ybx3*, were expressed over several cell populations. We observed that *Cldn3* is the TJ gene with the highest mRNA expression in hepatocytes and cholangiocytes (Figure 1C and D). Confocal Z-stack imaging showed that claudin-3 protein was localized with particularly high abundance at the hepatocyte canalicular membrane (Figure 1E and Supplementary Video 1) and had strong expression on the luminal membranes of cholangiocytes (Figure 1F). By immunofluorescence, we observed that claudin-3 protein has a zoned expression pattern in the liver, with the highest staining intensity in the pericentral region (Figure 1G). In summary, our scRNA-seq and immunofluorescence data show that claudin-3 is a prominent hepatic TJ protein that is found predominantly on canalicular membranes of pericentral hepatocytes and on the membranes of ductular cholangiocytes.

Effect of Claudin-3 Deletion on Liver Histology and TJ Integrity

We next assessed if claudin-3 contributes to normal liver homeostasis and function by studying mice with global claudin-3 knockout.²⁷ We first verified that *Cldn3*^{-/-} mice had no claudin-3 protein expression and confirmed the specificity of the claudin-3 antibody by Western blot and by immunostaining of liver tissue (Figure 2A and B). The livers of *Cldn3*^{-/-} mice had no macroscopic anatomic abnormalities (Figure 2C) and the liver's histology was unremarkable compared with age-matched littermate controls (Figure 2D). Furthermore, we could not detect gaps or discontinuities at TJs by electron microscopy (Figure 2E). There was also no difference in collagen deposition in male compared with female *Cldn3*^{-/-} livers (Figure 2F and G). Serum analysis showed no difference in alanine aminotransferase (ALT)

Abbreviations used in this paper: ALP, alkaline phosphatase; ALT, alanine-aminotransferase; AST, aspartate-aminotransferase; CA, cholic acid; DAPI, 4',6-diamidino-2-phenylindole; mRNA, messenger RNA; PBS, phosphate-buffered saline; pHH3, phosphohistone H3; PHx, partial hepatectomy; qPCR, quantitative polymerase chain reaction; scRNA-seq, single-cell RNA sequencing; TCA, taurocholic acid; TJ, tight junction; UMI, unique molecular identifiers.

 Most current article

© 2021 The Authors. Published by Elsevier Inc. on behalf of the AGA Institute. This is an open access article under the CC BY-NC-ND license (<http://creativecommons.org/licenses/by-nc-nd/4.0/>).

2352-345X/\$36.00

<https://doi.org/10.1016/j.jcmgh.2021.04.003>

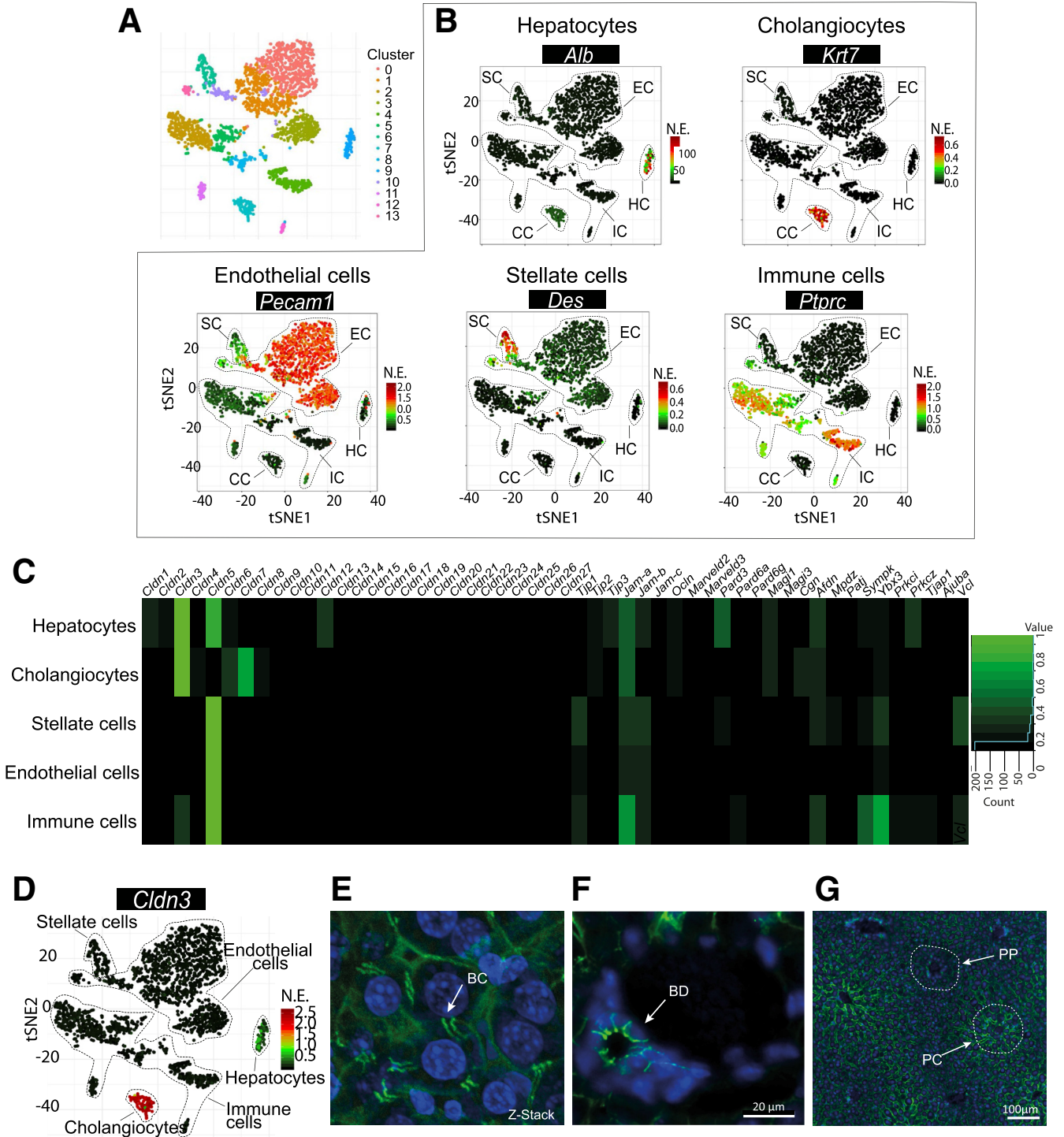
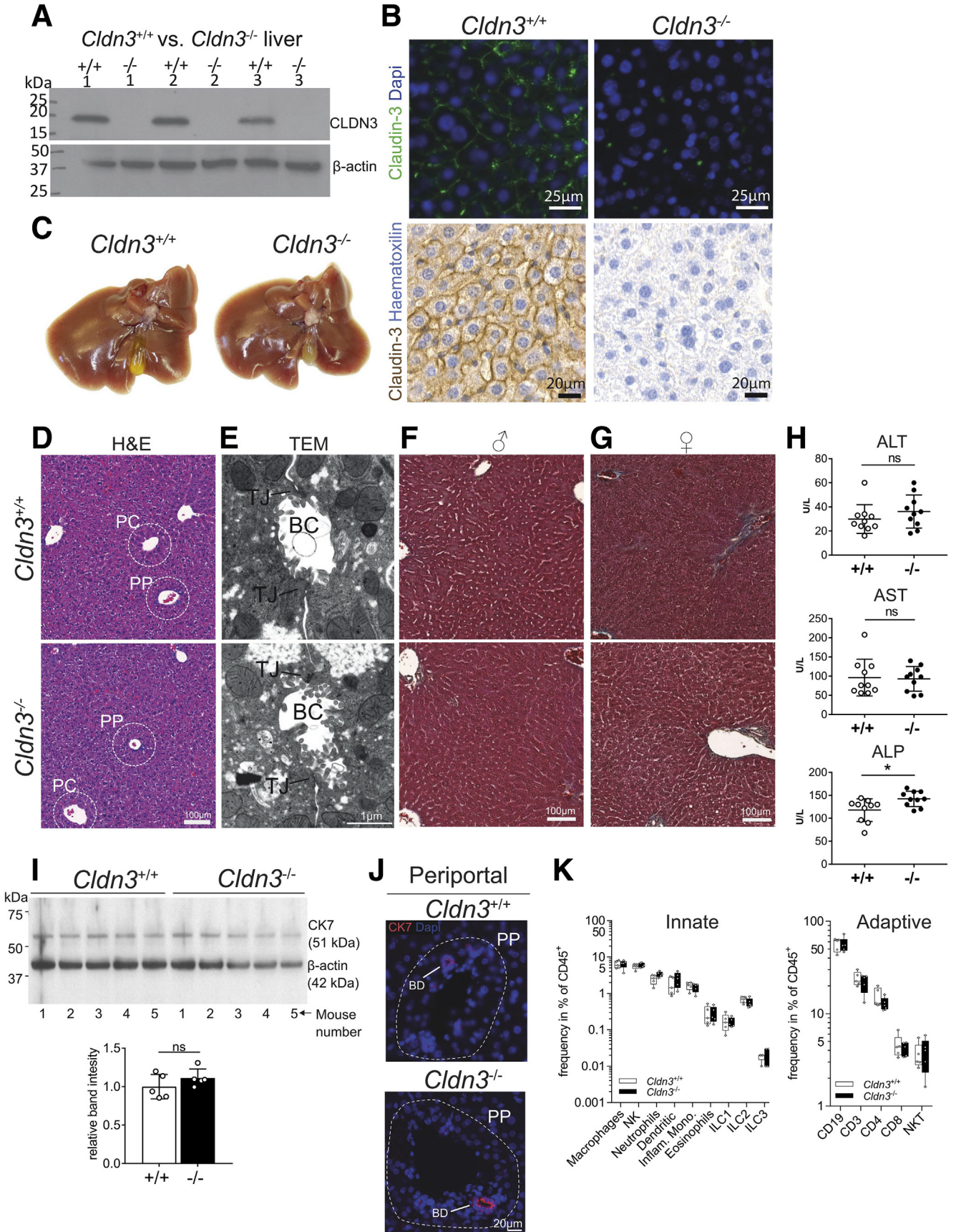


Figure 1. Cell type-specific analysis of TJ gene expression in a native mouse liver shows high expression of claudin-3 in hepatocytes and cholangiocytes. (A) Unsupervised clustering of the scRNA-seq data used for cell classification. (B) t-Distributed stochastic neighbor embedding (tSNE) plots depicting the expression of marker genes to define different hepatic cell populations: hepatocytes (HC), cholangiocytes (CC), stellate cells (SC), immune cells (IC), endothelial cells (EC). (C) Heatmap of scRNA-seq data depicting cell type-specific expression of hepatic TJ genes. Expression was normalized by cell type. (D) tSNE plot depicting the expression of *Cldn3*. (E) Three-dimensional reconstruction of a 30- μ m-thick confocal z-stack section stained for claudin-3 immunofluorescence (green), DAPI (blue) in mouse liver tissue. (F) Anti-claudin-3 centered on a bile duct. (G) Lower-magnification image showing zoned claudin-3 expression in the murine liver. (E–G) The microscope used for fluorescent image acquisition was a panoramic 250 Flash III, 3DHISTECH, panoramic scanner software, with a 40 \times objective. BC, bile canaliculus; BD, bile duct; NE, normalized expression; PC, pericentral zone; PP, periportal zone.



and aspartate aminotransferase (AST) levels, but slightly higher levels of alkaline phosphatase (ALP) in *Cldn3*^{-/-} livers, with 142.3 ± 15.8 U/L compared with 117.8 ± 23.3 U/L in *Cldn3*^{+/+} livers (Figure 2H). It has been described that loss of TJ integrity may cause inflammation and ductular reactions as a result of the cytotoxic effect of bile acid leakage.²⁸ Confirming our observation of intact TJ structures in *Cldn3*^{-/-} livers, we did not observe an increase in cytokeratin 7 (CK7), a marker for ductular reactions (Figure 2I and J) or an increase in the frequency of innate or adaptive immune cells in the livers (Figure 2K). In summary, we did not observe any gross alterations in liver histology or signs of loss of TJ integrity in *Cldn3*^{-/-} mice.

Claudin-3 Deletion Represses Metabolism and Bile Synthesis Gene Expression

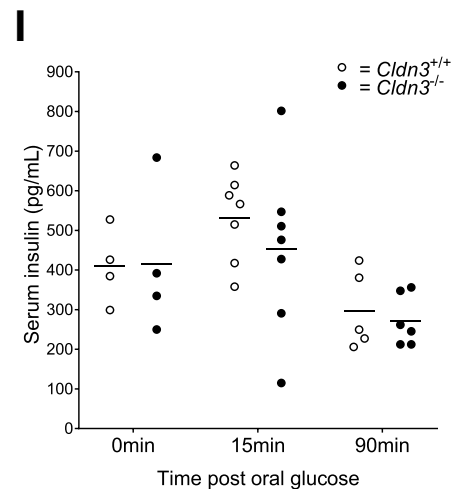
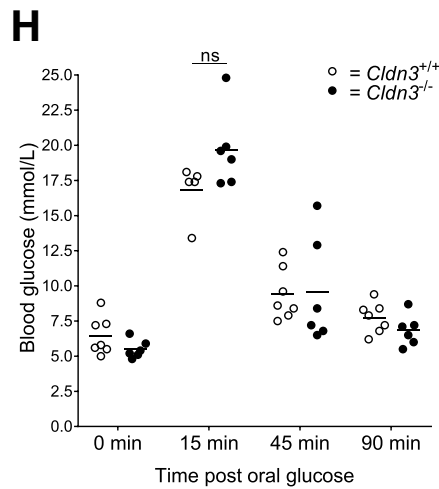
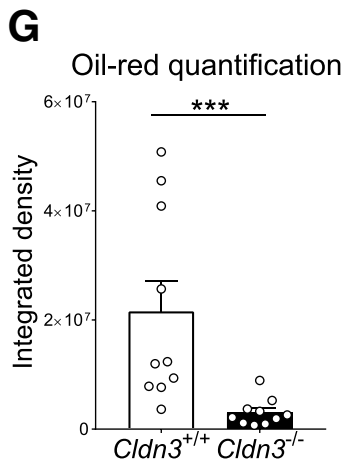
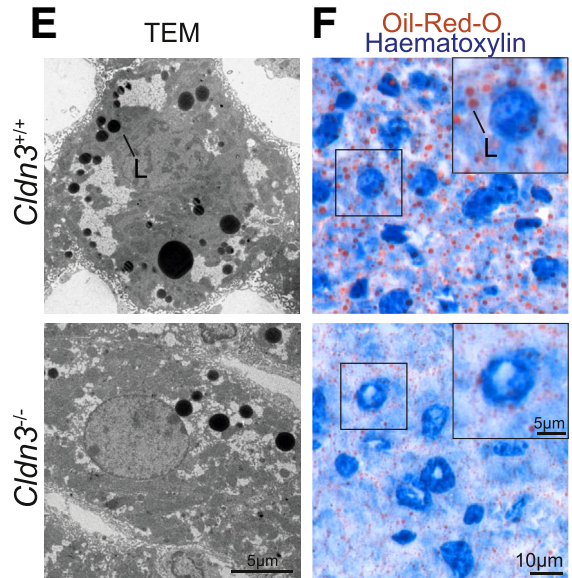
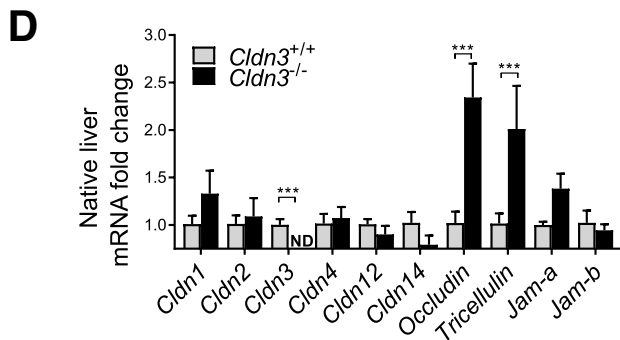
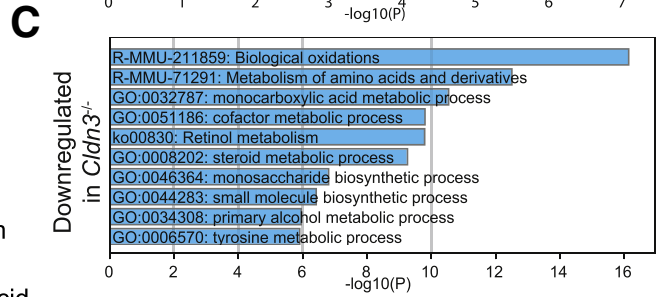
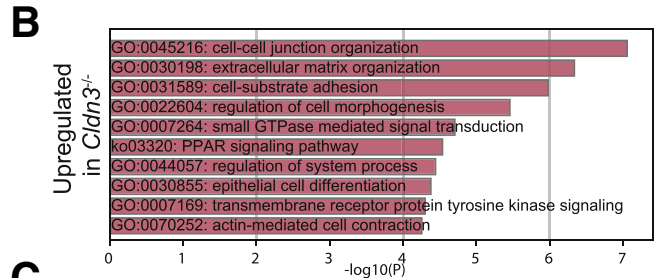
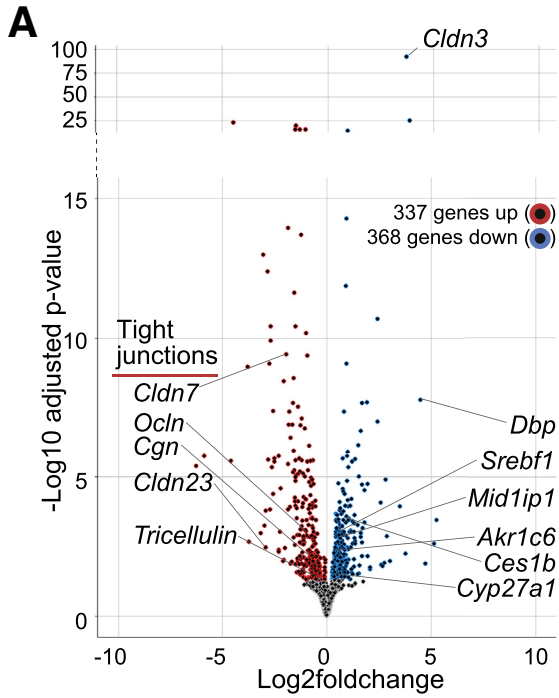
Questioning the absence of an overt phenotype by loss of claudin-3, we next checked if there were any overall changes in gene expression in *Cldn3*^{-/-} livers. RNA-seq analysis showed that there were 705 differentially expressed genes between wild-type and *Cldn3*^{-/-} livers, of which 337 genes were up-regulated, and 368 genes were down-regulated (Figure 3A). Genes related to cell adhesion and cell junctions were up-regulated significantly in *Cldn3*^{-/-} livers, for example, there was higher expression of *Ocln* (Occludin), *Tricellulin* (Marveld2), *Cldn7*, *Cldn23*, and *Cgn* (Figure 3A and B). The most important changes were verified by comparative real-time quantitative polymerase chain reaction (qPCR) (Figure 3D). From the RNA-seq data, we also observed a significant down-regulation of genes and pathways related to metabolism, including fatty acid-, amino acid-, bile acid-, and lipid-related gene expression in *Cldn3*^{-/-} livers (Figure 3A and C). This observation was consistent with the low amount of lipid droplets in *Cldn3*^{-/-} hepatocytes, as seen by electron microscopic and quantified Oil-red-O staining (Figure 3E–G). We next questioned the possible cause for repressed lipid metabolism in *Cldn3*^{-/-} livers. Glucose is one of the main drivers of de novo lipogenesis in the liver, which requires its efficient absorption in the intestine.²⁹ Because past reports have shown that

Claudin-3 also is expressed in the intestine,²⁴ we hypothesized that an inefficient baseline glucose absorption within the intestine may explain the down-regulation in lipid metabolism in *Cldn3*^{-/-} mice. However, baseline blood glucose levels did not differ significantly, and *Cldn3*^{-/-} mice showed a similar absorption and clearance after oral glucose challenge (2 mg/g bodyweight) when compared with *Cldn3*^{+/+} mice (Figure 3H). Accordingly, serum insulin levels were not significantly different between *Cldn3*^{+/+} and *Cldn3*^{-/-} in the oral glucose tolerance test (Figure 3I). Taken together, we observed many deregulated genes in *Cldn3*^{-/-} livers, including a compensatory increase of TJ gene expression and a repressive effect on metabolic processes in the liver.

Effect of Claudin-3 Deletion in Aged Animals

Because we observed a repression of lipid metabolism in *Cldn3*^{-/-} mice, we next questioned how they respond to the metabolic challenge of aging. It has been well described that senescence-related events that come with advanced age lead to increased accumulation of lipids and triglycerides in the liver.^{30–32} We first compared liver tissue of 12-week-old and 52-week-old mice and did not observe a change in hepatic claudin-3 protein levels resulting from age (Figure 4A). The bodyweight of *Cldn3*^{+/+} vs *Cldn3*^{-/-} mice was similar over time, while the liver-to-bodyweight ratio of 52-week-old *Cldn3*^{-/-} mice was slightly higher (Figure 4B and C). Liver damage markers ALT and AST did not differ (Figure 4D), however, we observed the same trend of increased ALP in aged *Cldn3*^{-/-} that was present in young animals (Figures 4D and 2H). In aged mice, there was no difference in collagen deposition owing to loss of claudin-3 expression (Figure 4E). We next compared the transcriptomic profile of young vs aged *Cldn3*^{+/+} and *Cldn3*^{-/-} mice by RNA-seq. In young animals there were differences owing to the loss of claudin-3 expression, however, the metabolic challenge of age was stronger than the effect of the loss of claudin-3 in aged animals (Figure 4F). Analysis of differentially expressed genes showed that in both *Cldn3*^{+/+} and *Cldn3*^{-/-} aged animals there was a profound down-regulation of metabolic pathways including fatty acid metabolism and

Figure 2. (See previous page). Effect of claudin-3 loss on liver morphology and TJ structure integrity. Mice with global claudin-3 knockout were generated as described in the Methods section. (A) Anti-claudin-3 Western blot on whole-liver tissue lysates of *Cldn3*^{+/+} and *Cldn3*^{-/-} mice. β -actin for loading control. No claudin-3 was detected in *Cldn3*^{-/-} samples, and only a single specific band was seen in *Cldn3*^{+/+} mice (n = 3). (B) Anti-claudin-3 immunofluorescence (green; DAPI in blue), and immunohistochemistry in *Cldn3*^{+/+} and *Cldn3*^{-/-} liver tissue. Claudin-3 staining was absent in the *Cldn3*^{-/-} samples. (C) Photographs of native *Cldn3*^{+/+} and *Cldn3*^{-/-} livers. (D) H&E staining. (E) Transmission electron microscopy (TEM) images centered on bile canaliculi. (F and G) Masson trichrome staining of female and male liver tissue. (H) Serum AST, ALT, and ALP levels in *Cldn3*^{-/-} vs *Cldn3*^{+/+} mice (n = 10, means \pm SD, **P* < .05, unpaired *t* test). (I) Anti-CK7 Western blot on whole-liver tissue of native *Cldn3*^{+/+} and *Cldn3*^{-/-} mice. Band intensities were normalized to β -actin (n = 5, *t* test, *Cldn3*^{+/+} band intensities were compared with their group average). (J) Anti-CK7 immunofluorescence (red) in periportal liver tissue, and DAPI in blue. Representative images were taken. Quantification of the Western blot below (n = 5, bars represent means \pm SEM, unpaired *t* test). (K) Fluorescence-activated cell sorting analysis of innate and adaptive immune cell populations. The frequency of immune cells was not different in *Cldn3*^{+/+} and *Cldn3*^{-/-} native livers (n = 5, unpaired *t* test). The microscopes used for image acquisition in this figure were an immunofluorescence Leica DMI4000B with a 20 \times objective with Leica advance fluorescence software, and an immunohistochemistry panoramic 250 Flash III, 3DHISTECH, panoramic scanner software, with a 20 \times objective; electron microscopy, Philips CM 12. BC, bile canaliculus; CK7, cytokeratin 7; ILC, innate lymphoid cells; Inflamm. Mono., inflammatory monocytes; NK, natural killer cells; NKT, natural killer T-cells; PC, pericentral area; PP, periportal area.



catabolic processes and an up-regulation of inflammation and immune responses (Figure 4G and H). However, when aged *Cldn3*^{+/+} and *Cldn3*^{-/-} were compared, only a few genes were significantly different, particularly *Apol9a*, *Apol9b*, and *Cyp26a1*, genes related to cholesterol and lipid metabolism, which were lower in *Cldn3*^{-/-} mice (Figure 4I).

Following results from our RNA-seq data and reports that age leads to impaired lipid metabolism,³⁰⁻³³ we were able to confirm a significant increase of lipid content in aged livers, however, *Cldn3*^{-/-} mice had a lower lipid content compared with *Cldn3*^{+/+} mice (Figure 4J) as we observed previously in young animals (Figure 3E-G). For further validation of the inflammatory phenotype that our gene expression data indicated (Figure 4G and H), we showed that the frequency of total hepatic lymphocytes increased with age in both groups (Figure 4K). In summary, all aged animals had higher amounts of hepatic lipids and liver inflammation compared with young animals, and aged *Cldn3*^{-/-} mice retained lower hepatic lipid levels compared with wild-type controls.

Impairment of the Blood-Biliary Barrier in *Cldn3*^{-/-} Livers

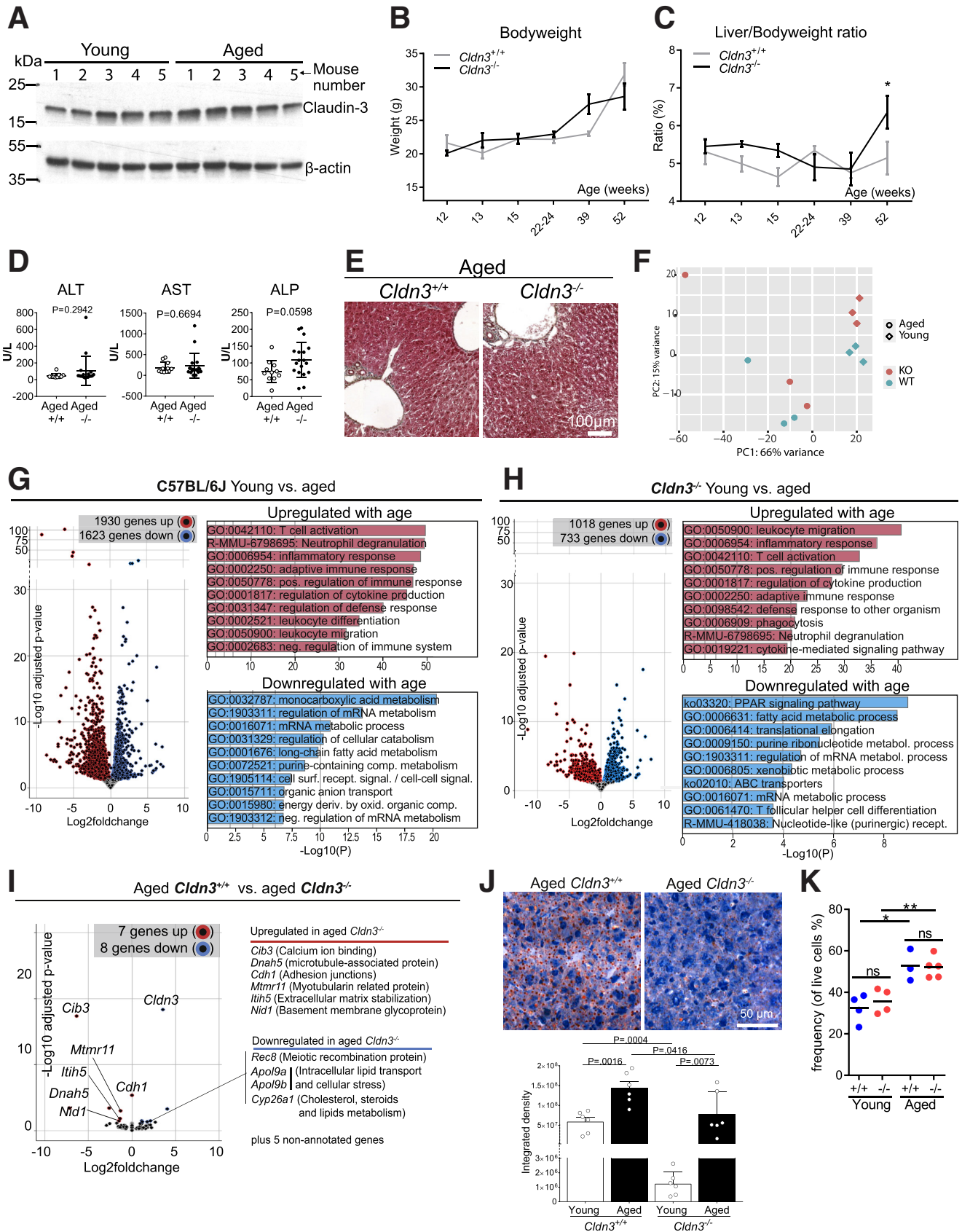
Our RNA-seq analysis showed that genes involved in bile acid metabolism such as *Cyp27a1*, *Ces1b*, and *Akr1c6* were down-regulated in *Cldn3*^{-/-} mice (Figure 3A). We therefore questioned if there are lower bile acid levels in *Cldn3*^{-/-} mice by measuring their abundance in liver tissue and serum by liquid chromatography–tandem mass spectrometry. Lower total bile acid levels were measured in the liver tissue, while total bile acids were higher in the serum of *Cldn3*^{-/-} mice compared with *Cldn3*^{+/+} mice (Figure 5A and B). The proportion of primary bile acids was higher in the serum of *Cldn3*^{-/-} mice (Figure 5B). Importantly, individual bile acids were significantly less concentrated in the liver (Figure 5C), and more highly concentrated in the serum (Figure 5D). This included cholic acid (CA), taurocholic acid (TCA), taurochenodeoxycholic acid, conjugated forms of muricholic acids and the secondary bile acid tauro-7-oxolithocholic acid (Figure 5C and D). The other individual bile acids did not significantly differ between *Cldn3*^{+/+} and *Cldn3*^{-/-} in the

liver or serum (Figure 5E and F). The change in bile composition prompted us to check the appearance of the gallbladders. We did not find any incidence of gallstones in the gallbladders and observed that *Cldn3*^{-/-} gallbladders were lighter in color compared with wild-type organs (Figure 6A). As a possible contributing factor to the change in circulating bile acid composition, we checked in the RNA-seq data if the expression of transporters is altered in *Cldn3*^{-/-} mice (Figure 6B). The expression of transporter transcripts that showed a trend in the RNA-seq results were verified by real-time qPCR (Figure 6C). We observed higher expression of *Ost1-β* (Slc51b), and a trend for higher *Asbt* (Slc10a2) levels in *Cldn3*^{-/-} mice (Figure 6B and C). Because the nuclear transcription factor Farnesoid X-receptor is a regulator of bile transporters,³³ we checked *Fxr* and downstream target expression (Figure 6D). However, we found only a modest alteration of the Farnesoid X-receptor targets *Bacs* (Slc27a5) and *Apoa1* (Figure 6D). Finally, we tested the expression of *Fgf15* in the ileum (Figure 6E), but did not observe a difference in *Cldn3*^{-/-} when compared with *Cldn3*^{+/+} animals. In conclusion, our results suggest that the biliary barrier of *Cldn3*^{-/-} mice is partially impaired and alterations in bile acid transporter expression also may contribute to the change in hepatic bile acid levels.

Hepatic Proliferation Is Impaired in *Cldn3*^{-/-} Mice After Partial Hepatectomy

The observations that loss of claudin-3 expression affects liver metabolism, particularly lipid metabolism and hepatic bile acid content, raised the question of whether claudin-3 is important for the liver's response to injury. Therefore, we tested if the loss of claudin-3 expression altered the liver's ability to regenerate after PHx. We observed a time-dependent regulation of claudin-3 mRNA and protein in wild-type animals in response to PHx. *Cldn3* expression was decreased after 3 and 6 hours and increased above baseline levels starting at 24 hours (Figure 7A). We validated this observation by immunofluorescent staining (Figure 7B) and Western blot (Figure 7C and D). The zoned expression pattern that was present in native liver tissue was lost at 48 hours after PHx (Figure 7B). PHx leads

Figure 3. (See previous page). Repressed lipid metabolism in *Cldn3*^{-/-} mice. (A) Volcano plot showing up-regulated and down-regulated genes (red circles and blue circles, respectively) in *Cldn3*^{-/-} compared with *Cldn3*^{+/+} native liver tissue. RNA-seq analysis was performed by DESeq2 (n = 3 for *Cldn3*^{-/-} and n = 4 for *Cldn3*^{+/+}, differential expression significance threshold: P value adjusted < .05). A total of 15,148 nonsignificantly regulated genes are shown as grey circles. A selection of significantly regulated genes related to TJs, metabolism, or bile synthesis is annotated. Metascape analysis of the (B) top 10 up-regulated and (C) top 10 down-regulated gene pathways within the data set of panel A. (D) Comparative real-time qPCR in native liver tissue. The fold change in mRNA expression of *Cldn3*^{-/-} was obtained by comparison with *Cldn3*^{+/+} mice (n = 4, unpaired t test, ***P < .001, *Cldn3*^{+/+} control $\Delta\Delta\text{CT}$ values = $\Delta\text{CT}(\text{individual}) - \Delta\text{CT}(\text{group average})$, bars represent the means \pm SEM). (E) Transmission electron microscopy (TEM) images of representative hepatocytes. Lipid droplets (L) appeared less in number and size in *Cldn3*^{-/-} hepatocytes. (F) Oil-red-O staining showing a lower amount of lipid droplets (L) in *Cldn3*^{-/-} liver tissue. (G) Quantification of images from randomly chosen regions of Oil-red-O-stained native liver tissue (n = 10, bars represent means \pm SEM, ***P < .001, Mann-Whitney test). (H) Oral glucose tolerance test. D-glucose (2 mg/g bodyweight) was given by oral gavage and blood glucose levels were determined at the indicated times (n = 7 for *Cldn3*^{+/+} and n = 6 for *Cldn3*^{-/-}, exception for t = 15 min *Cldn3*^{+/+} n = 5, unpaired Student t test). (I) Enzyme-linked immunosorbent assay test for serum insulin levels at the indicated times after oral glucose challenge. No significant differences were observed (0 min, n = 4; 15 min, n = 7; 90 min, n = 5 [*Cldn3*^{+/+}] and n = 6 [*Cldn3*^{-/-}], unpaired Student t test). Microscopes used for image acquisition in this figure for Oil-red-O staining: panoramic 250 Flash III, 3DHISTECH, panoramic scanner software, with a 40 \times objective; electron microscopy, Philips CM 12. ND, nondetectable.



to high pressure and mechanical stress within the first hours after resection,³⁴ therefore, we checked if the increased stress affected the integrity of TJs in *Cldn3*^{-/-} mice. However, by electron microscopy, we did not find any gaps or other obvious membrane impairments after 6 hours after PHx in either *Cldn3*^{+/+} or *Cldn3*^{-/-} (Figure 7E). In agreement, there were no signs of an inflammatory reaction based on cytokine secretion or cytokeratine expression (Figure 7F–H), and the frequencies of immune cells were not significantly different in regenerating *Cldn3*^{-/-} livers (Figure 7I).

We next determined the proliferative scores 48 hours after PHx. The percentage of Ki67-positive hepatocytes was 76% ± 4% in *Cldn3*^{+/+} mice compared with 49% ± 5% in *Cldn3*^{-/-} mice ($P < .01$) (Figure 8A). For the mitosis marker phosphohistone H3 (pHH3), *Cldn3*^{+/+} livers had 32% ± 3% pHH3-positive nuclei, compared with only 15% ± 1% in *Cldn3*^{-/-} livers ($P < .01$) (Figure 8B). Supporting these results, the transcription of *Foxm1* increased 43- ± 3-fold over controls in *Cldn3*^{+/+}, and only 16- ± 2-fold in *Cldn3*^{-/-} livers ($P < .001$) (Figure 8C). Similarly, *Ccnb1* and *Birc5* were significantly less transcribed in *Cldn3*^{-/-} mice at 48 hours after PHx. The proliferation inhibitor *p21* (*Cdkn1a*), on the other hand, was expressed higher in *Cldn3*^{-/-} mice at 24 and 48 hours after PHx ($P < .05$ and $P < .01$, respectively) (Figure 8C). At 72 hours after PHx, the proliferation scores and the expression of genes regulating cell proliferation did not differ between *Cldn3*^{+/+} and *Cldn3*^{-/-} mice. RNA-seq data of liver tissue 48 hours after PHx supported the immunofluorescence and real-time qPCR data (Figure 8D). Genes associated with cell division, cell-cycle regulation, cholesterol synthesis, and glucose metabolism were expressed at a lower level in regenerating *Cldn3*^{-/-} livers (Figure 8D and F), whereas genes related to circadian rhythm, negative regulation of metabolism, lipid catabolism, and calcium ion binding, as well as others, were found to be

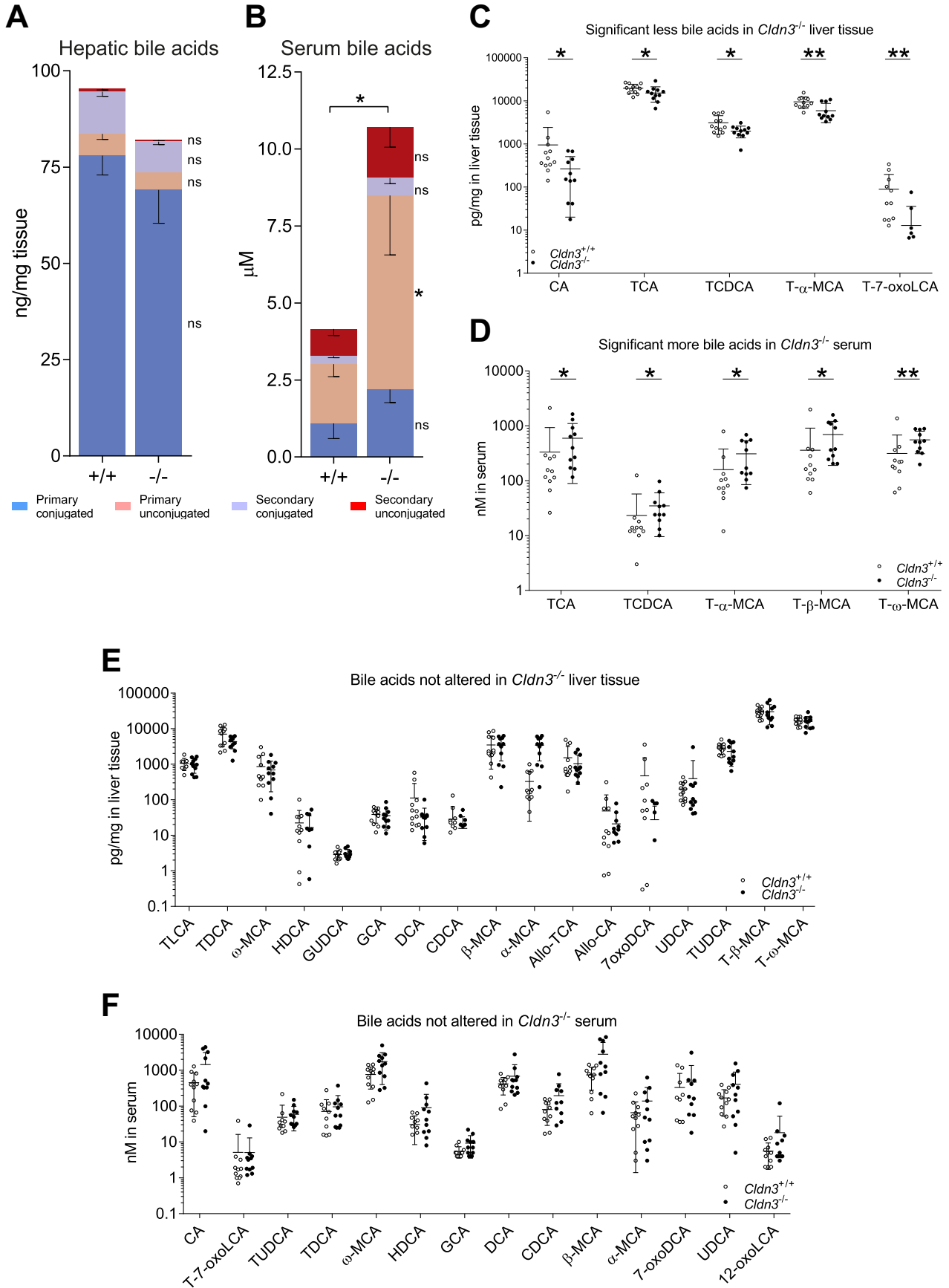
up-regulated (Figure 8D and E). Taken together, we saw that *Cldn3*^{-/-} mice had an impairment in proliferation after PHx.

Discussion

Several studies have described hepatic TJ proteins and their function within the blood-biliary barrier.^{4,14,16,18,22} By using scRNA-seq, we expanded the available information on hepatic TJ gene expression by describing their abundance in the various cell populations of the liver. We found the expected expression pattern for some genes, for example, *Cldn1*, *Cldn2*, *Cldn5*, and *Cldn7*,^{18,35–41} and, interestingly, we observed expression of *Cldn5*, *Jam-a*, *Jam-b*, *Afdn*, *Sympk*, and *Ybx3* in stellate and immune cells, suggesting a role of TJ genes outside the blood-biliary barrier. Our scRNA-seq data support that *Cldn3* is one of the most highly expressed TJ genes in the mouse liver with its mRNA and protein expressed predominantly in hepatocytes and cholangiocytes.^{18,22,40–42} Within a liver lobule, there is a discernable metabolic zonation,^{43,44} and bile acid synthesis is highest in the first 3 hepatocyte cell layers around the central veins.⁴⁵ This correlates with the high level claudin-3 expression we observed in the pericentral region, suggesting that the liver may express higher levels of claudin-3 to ensure a tightly sealed blood-biliary barrier in the location of higher bile acid concentrations.

To study the consequence of loss of claudin-3 expression, we used *Cldn3*^{-/-} mice, however, the phenotype we observed was milder than what was reported originally.²² For example, in our study, there was a very moderate increase of total serum bile acids and no gallstones were found even in aged animals.²² A possible explanation could be differences in environmental factors such as nutrition or microbiota.⁴⁶ Our transmission electron microscopy images support that hepatic TJs in *Cldn3*^{-/-} mice are intact because the membranes of adjacent cells are tightly sealed.²²

Figure 4. (See previous page). Metabolic challenging by aging leads to lower lipid accumulation in *Cldn3*^{-/-} liver. (A) Anti-claudin-3 Western blot on whole-liver tissue lysate of young (12 weeks) and aged (52 weeks) wild-type mouse livers. β -actin was used as loading control (n = 5). (B) Body weight measurements in *Cldn3*^{+/+} (gray line) vs *Cldn3*^{-/-} (black line) mice at the indicated age of life (12 weeks, n = 7 [*Cldn3*^{+/+}] and n = 11 [*Cldn3*^{-/-}]; 13 weeks, n = 6 [*Cldn3*^{+/+}] and n = 4 [*Cldn3*^{-/-}]; 15 weeks, n = 5 [*Cldn3*^{+/+}] and n = 7 [*Cldn3*^{-/-}], 22–24 weeks, n = 5; 39 weeks, n = 3 [*Cldn3*^{+/+}] and n = 4 [*Cldn3*^{-/-}], 52 weeks, n = 3 [*Cldn3*^{+/+}] and n = 5 [*Cldn3*^{-/-}]). No significant differences were observed at any age (unpaired *t* test). (C) Liver-to-bodyweight ratio was measured (12 weeks, n = 7 [*Cldn3*^{+/+}] and n = 11 [*Cldn3*^{-/-}]; 13 weeks, n = 6 [*Cldn3*^{+/+}] and n = 4 [*Cldn3*^{-/-}]; 15 weeks, n = 5 [*Cldn3*^{+/+}] and n = 6 [*Cldn3*^{-/-}]; 22–24 weeks, n = 5; 39 weeks, n = 3 [*Cldn3*^{+/+}] and n = 4 [*Cldn3*^{-/-}]; 39 weeks, n = 3; 52 weeks, n = 3 [*Cldn3*^{+/+}] and n = 5 [*Cldn3*^{-/-}]; * $P < .05$, unpaired *t* test). (D) Serum AST, ALT, and ALP levels in mice 1 to 2 years old. *Cldn3*^{-/-} vs *Cldn3*^{+/+} mice (n = 11 for *Cldn3*^{+/+} and n = 18 for *Cldn3*^{-/-}, means ± SD, * $P < .05$, unpaired *t* test). (E) Masson trichrome staining in aged mice. Representative image is shown (n = 3 and n = 4 for *Cldn3*^{+/+} and *Cldn3*^{-/-}, respectively). (F) Principal component analysis plot based on RNA-seq gene expression data of aged (circles) and young (diamonds) *Cldn3*^{+/+} (blue) and *Cldn3*^{-/-} (red) mice (n = 3 for both aged groups, n = 3 for young *Cldn3*^{-/-} and n = 4 for young *Cldn3*^{+/+} group). (G and H) Volcano plots and metascape analysis showing up-regulated and down-regulated genes and the top 10 up-regulated and down-regulated pathways in young (12 weeks) and aged (1.5–2 years) (G) C57BL/6 J mice and (H) *Cldn3*^{-/-} mice. RNA-seq analysis was performed by DESeq2 (n = 3 for both aged groups, n = 3 for young *Cldn3*^{-/-} and n = 4 for young *Cldn3*^{+/+} group, differential expression significance threshold: P value adjusted < .05). Genes or pathways with low expression in aged mice are shown in blue, and with high expression in aged mice are shown in red. (I) Volcano plot showing differential gene expression in aged *Cldn3*^{+/+} vs aged *Cldn3*^{-/-} mice, with regulated genes annotated next to it. Parameters of the differential gene expression as shown in panels G and H. (J) Oil-red-O staining on liver tissue sections. Quantification of images from randomly chosen regions below (n = 6, bars represent means ± SD, unpaired *t* test). (K) Fluorescence-activated cell sorting analysis comparing young and aged *Cldn3*^{+/+} and *Cldn3*^{-/-} mice (n = 4 in young, n = 3 in aged *Cldn3*^{+/+} and n = 5 in aged *Cldn3*^{-/-}, unpaired *t* test, * $P < .05$, ** $P < .01$). Microscopes used for image acquisition in this figure: Masson trichrome staining and Oil-red-O staining, panoramic 250 Flash III, 3DHISTECH, panoramic scanner software, with a 40× objective. KO, knockout; PC, pericentral; WT, wild-type.



Consequently, we could not detect morphologic changes or signs of inflammation or fibrosis owing to loss of claudin-3 expression. This lack of phenotype may be explained by the higher expression of other TJ-forming genes such as occludin and tricellulin, which may have functionally compensated for the loss of claudin-3.

However, by sequencing the livers of *Cldn3*^{-/-} mice we found significant repression in hepatic metabolism. There was a lower amount of lipid droplets in *Cldn3*^{-/-} livers and down-regulation of key genes related to lipogenesis including *Srebf1*.⁴⁷ A main activator of SREBF1 and its downstream targets is glucose.²⁹ We therefore tested if glucose uptake and insulin secretion are affected in *Cldn3*^{-/-} mice, which was not the case. However, we observed decreased expression of bile acid synthesis-involved genes including *Cyp27a1*⁴⁸ and *Akr1c6*.⁴⁹ In combination with the changed composition of the circulating bile acid pool in *Cldn3*^{-/-} mice, it is possible that altered bile metabolism negatively influenced the energy metabolism of the liver, because bile acids are important regulators of lipogenesis.^{50,51} The altered lipid metabolism in *Cldn3*^{-/-} prompted us to question how the mice respond to a metabolic challenge, which we induced by letting the mice age for up to 2 years. Of note, we did not observe a decrease in expression of claudin-3 protein in aged wild-type mice, as previously suggested.⁴² In aged livers, we observed the expected accumulation of hepatic lipids as well as inflammation and immune cell infiltrations. These events took place in *Cldn3*^{-/-} mice as well. When comparing the gene expression in aged *Cldn3*^{-/-} vs aged *Cldn3*^{+/+} mice by RNA-seq, we found a lower expression of lipid metabolism-related genes *Apol9a/b*⁵² and *Cyp26a1*⁵³ in the knockout animals. In conjunction, we also observed a lower amount of lipids in aged *Cldn3*^{-/-} compared with aged *Cldn3*^{+/+} liver. This implies that *Cldn3*^{-/-} mice respond differently to the metabolic challenge of age, accumulating fewer hepatic lipids. Both *Cldn3*^{+/+} and *Cldn3*^{-/-} mice showed a high lipid and inflammatory phenotype upon metabolic challenge by age, however, aged *Cldn3*^{-/-} mice again showed a phenotype of repressed lipid metabolism.

Because our differential gene expression data showed repression of bile acid synthesis-involved genes including *Cyp27a1*⁴⁸ and *Akr1c6*,⁴⁹ we also questioned if the composition of bile acids differs in *Cldn3*^{-/-} mice. Our results showed that *Cldn3*^{-/-} mice have a reduction in the concentration of hepatic CA, and its conjugated form TCA. In contrast, serum levels of TCA were higher in *Cldn3*^{-/-} mice, and there was a trend toward higher CA serum levels. Similarly, conjugated subtypes of a mouse-specific bile acid, muricholic acid, were decreased in the *Cldn3*^{-/-} liver, and

increased in the serum. The cause for the higher amount of serum bile acids could be owing to leaks of TJ barrier that are not visible by electron microscopy, or were owing to the slightly higher expression of the biliary exporter *Ost1-β*. Because bile acids are important for efficient nutrient digestion and lipid uptake,⁵⁴ we may speculate that the change in bile acid composition was a contributing factor to the repression in lipid metabolism of *Cldn3*^{-/-} livers. We next questioned whether the alterations in lipid metabolism and biliary barrier influenced the ability of the liver to regenerate. In fact, both efficient lipid supply^{55,56} and bile acid accumulation^{48,57} are required to settle the increased energy demand of hepatocytes during cell division. Interestingly, we observed an up-regulation of claudin-3 expression between 24 and 48 hours after PHx, which is in agreement with previous observations made in rats.⁵⁸ The increase of claudin-3 expression suggests that the biliary barrier needs to be tightened at this particular time after surgery. Possibly, claudin-3 retains bile acids to prevent hepatocellular damage, and/or to keep bile acids as liver regeneration-promoting signals.^{57,59,60} Our results showed that cell proliferation was decreased significantly in regenerating *Cldn3*^{-/-} livers, with approximately one-third less Ki67-positive and only half the amount of pHH3-positive cells at 48 hours after PHx. Because liver regeneration has high clinical relevance for treatment of hepatic malignancies and the repair of trauma,^{61,62} our results might be of interest for further investigations on the role of TJ proteins for optimal recovery after tissue loss.

Taken together, our data suggest that loss of claudin-3 leads to an impairment in lipid metabolism and an impaired biliary barrier in mice. Both of these phenotypes likely contribute to the suboptimal hepatic proliferation after PHx. However, we cannot exclude the possibility that claudin-3 is associated with signaling pathways that regulate the cell cycle. For example, claudin-3 is in direct and indirect contact with TJ adapter proteins that are upstream of transcription factors, including zonula occludens 1 (ZO-1)-associated nucleic acid binding protein (ZONAB), cellular myelocytomatosis protein (C-MYC), β-catenin, yes-associated protein 1 (YAP), and others.⁶³⁻⁶⁶ It will be of future interest to investigate the potential role of claudin-3 in the context of signaling pathways that control cell proliferation.

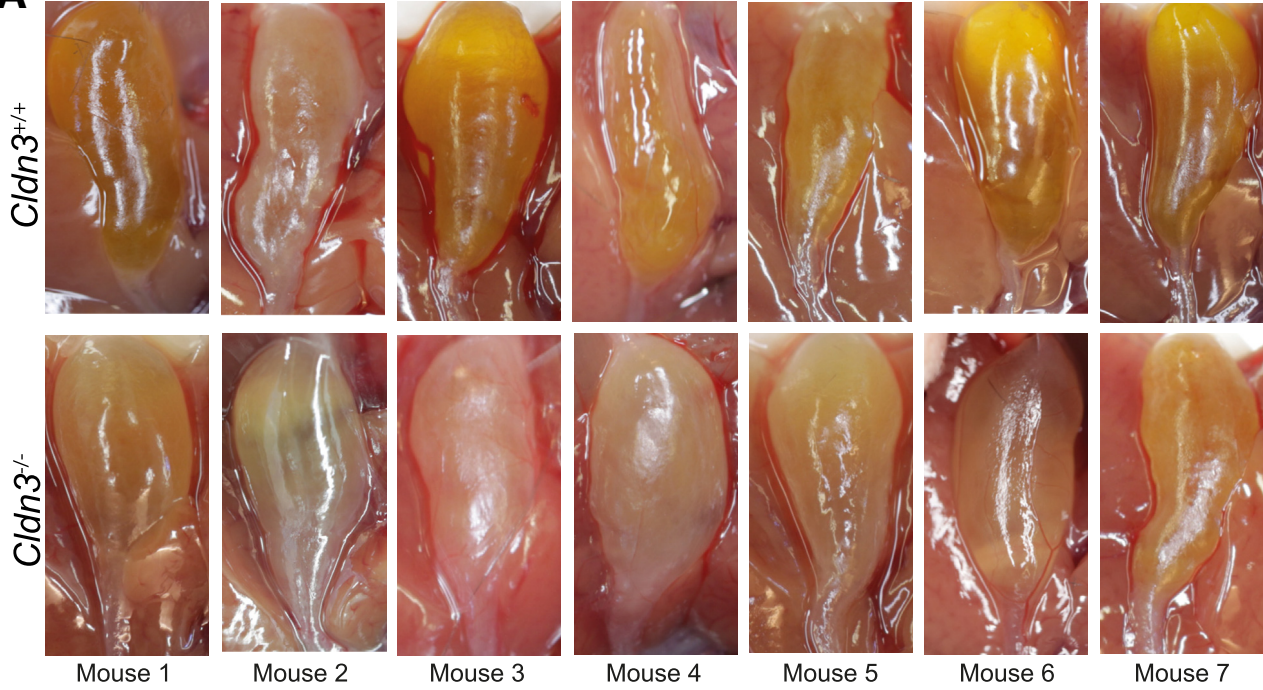
Materials and Methods

Generation of *Cldn3*^{-/-} Mice

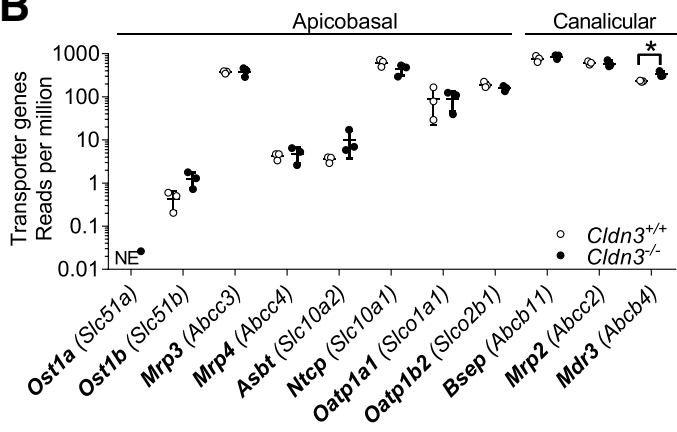
We described the generation of this strain with global claudin-3 knockout in detail in a previous publication.²⁷ In

Figure 5. (See previous page). Partial impairment of the *Cldn3*^{-/-} biliary barrier alters bile acid homeostasis. (A) Liquid chromatography–mass spectrometry (LC-MS) analysis of liver bile acids (n = 12/*Cldn3*^{+/+} and n = 11/*Cldn3*^{-/-}, means ± SEM, unpaired t test). (B) LC-MS analysis of serum bile acids (n = 11, means ± SEM, *P < .05, unpaired t test). (C) LC-MS analysis showing individual bile acid types in the liver (n = 12/*Cldn3*^{+/+} and n = 11/*Cldn3*^{-/-}, means ± SD, *P < .05, **P < .01 Mann–Whitney test). (D) LC-MS analysis showing individual bile acids in the serum (n = 11, means ± SD, *P < .05, **P < .01 Mann–Whitney test). (E and F) Bile acids that were not changed significantly in *Cldn3*^{+/+} vs *Cldn3*^{-/-} liver tissue or serum (n = 11, means ± SD, Mann–Whitney test). CDCA, chenodeoxycholic acid; DCA, deoxycholic acid; GCA, glycocholic acid; GUDCA, glyoursodeoxycholic acid; HDCA, hyodeoxycholic acid; MCA, muricholic acid; oxoLCA, oxo-lithocholic acid; TCDCA, taurohyodeoxycholic acid; TDCA, tauro-deoxycholic acid; TLCA, tauro-lithocholic acid; TUDCA, tauro-ursodeoxycholic acid; UDCA, ursodeoxycholic acid.

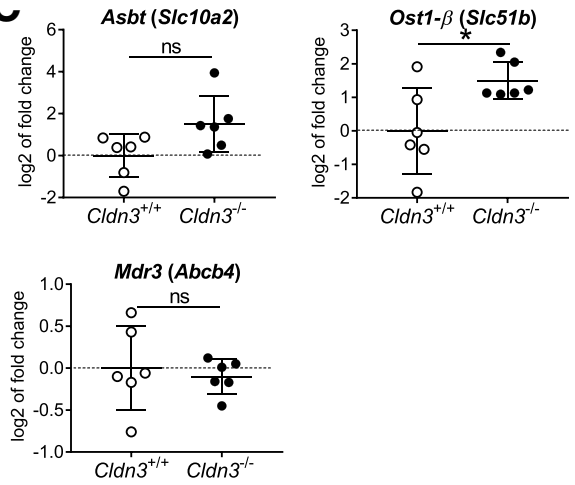
A



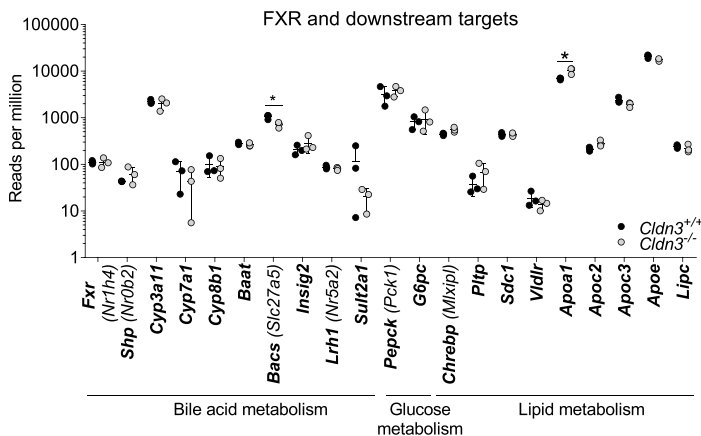
B



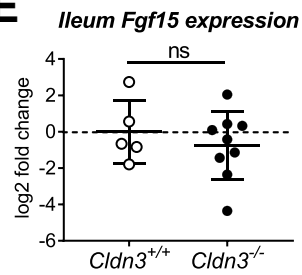
C



D



E



embryonic stem cells, we used a PGK neo cassette to replace most of the claudin-3 coding region, except for the last 30 nucleotides of the open reading frame. This created a knockout allele and prevented claudin-3 peptide formation, which we confirmed by Western blot and immunofluorescence (Figure 2A and B). By interbreeding heterozygous parents, we created homozygous *Cldn3*^{-/-} mice at almost Mendelian ratios (23.5%). To homogenize the C57BL/6J genetic background, we backcrossed for more than 10 generations.

Animal Housing and PHx Surgery

Both experimental C57BL/6J *Cldn3*^{-/-} and control C57BL/6J *Cldn3*^{+/+} mice were born and raised within the same animal housing facility. Mice were housed under specific pathogen-free conditions at 22°C, 55% relative humidity, with free access to chow and water, and in a 12-hour, light-cycle controlled room. Green Line individually vented cages (Tecniplast, Hohenpeißenberg, Germany) were used at positive pressure. Safe Aspen (S-Aspen-09322; JRS, Horn, Switzerland) cage bedding was used. Animal cages contained enrichment and activation tools such as plastic mouse house (Tecniplast), Nestlet or Sizzle nests (Plexx, Elst, Netherland), and Pura Crinkle Brown Kraft Paper (Labodia, Niederglatt, Switzerland). Mice were fed a standard dry pellet cereal-based diet (10343200PXV20; Granovit, Switzerland). Interventions were performed during the light phase in 12- to 18-week-old male and female mice (weight, ~18–22 g). Liver regeneration was studied using a standard model of PHx by removing the left and medial liver lobes as previously described.⁶⁷ Mice were killed by exsanguination under deep anesthesia. All mouse experiments were performed with the approval of the Veterinary Office of the Canton Bern (permit BE51/18), according to the guidelines of good animal practice as defined by the Office of Laboratory Animal Welfare, and adhering to the standards of the national centre for the replacement refinement and reduction of animals in research guidelines (<https://www.nc3rs.org.uk/arrive-guidelines>).

Single-Cell RNA Sequencing

The unique molecular identifiers (UMI) matrix of our recently published scRNA-seq was downloaded (GEO accession number: GSE134134).²⁶ We removed cells with more than 15% UMIs coming from mitochondrial genes and cells with more than 25% UMIs coming from globin genes. In addition, a cell containing an abnormally high number of UMIs (110,270) was excluded. Next, we removed genes that were not expressing at least 2 reads in 2 genes. After data preprocessing, the UMI matrix was processed as previously

described.²⁶ Shortly, we transformed the UMI matrix into a Seurat object (Paul Hoffman, Satija Lab, New York Genome Center, New York) with Seurat 2 (PMID: 31178118). The data of the Seurat object were log-normalized, the variable genes were identified, and the data were scaled. Next, we computed the principal component analysis with the R (RStudio PBC, Boston, MA) function *RunPCA*, we identified the clusters with the R function *FindClusters* with *dims.use=1* and *resolution=1*. Finally, we computed the t-distributed stochastic neighbor embedding coordinates with the R function *RunTSNE* with *dims.use=1:8*.

Cell identification. In Figure 1B, we show the expression of the following cell population markers (Figure 1B shows markers): hepatocytes: *Alb* (shown), *Apoa1*, *G6pc*, *Hnf4a*, *Asgr1*, *Mup3*, *Pck1*; cholangiocytes: *Krt7* (shown), *Krt19*, *Muc1*, *St14*; endothelial cells: *Pecam1* (shown), *Dpp4*, *Oit3*, *Gpr182*, *Lyve1*, *Ushbp1*, *Tek*; stellate cells: *Des* (shown), *Reln*, *Rbp1*, *Prnp*, *Vcl*, *Hhip*, *Col1A1*; and immune cells: *Ptprc* (*Cd45*) (shown). Based on clustering and gene expression, we defined cluster 9 as hepatocytes; cluster 7 as cholangiocytes; clusters 2, 4, 5, 8, 11, and 12 as immune cells; clusters 0, 1, 3, 10, and 13 as endothelial cells; and cluster 6 as stellate cells (Figure 1A).

Data visualization. To display the gene expression, the preprocessed UMI matrix was normalized with the function *library.size.normalization* of the R package *Magis*.⁶⁸

The dropout correction was performed with the R function *magic* with parameters *genes="all_genes"*. The dropout corrected data were displayed on the t-distributed stochastic neighbor embedding plots.

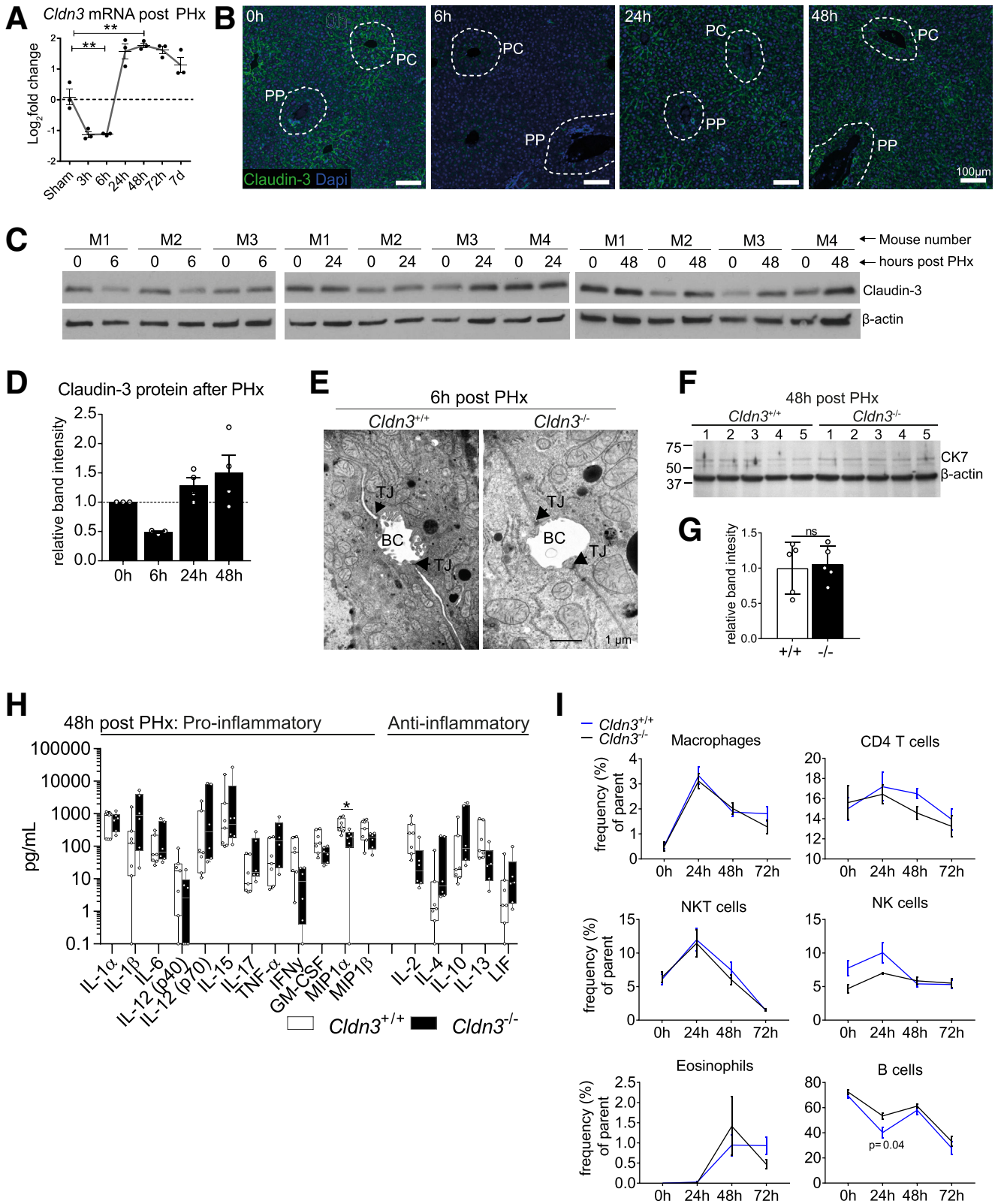
Heatmap. The unsupervised clusters containing the same cell types were merged and we averaged the UMI expression in each cell type, the average expression of each gene was normalized from 0 to 1, $f(x) = (x - \min(x)) / (\max(x) - \min(x))$, and represented as a heatmap with the R package *gplots*.

Histology

Immunohistochemistry and immunofluorescence. Paraffin-embedded liver tissue was sectioned at a thickness of 6 μm for conventional imaging or 30 μm for confocal z-stack imaging. Slides were deparaffinized and hydrated in a xylol and ethanol series. For nuclear staining, membrane permeabilization was performed by 20-minute incubation in phosphate-buffered saline (PBS)-Triton X-100 (0.4%) (1.09468.0100 and 108603; Merck, Darmstadt, Germany).

Antigen retrieval was performed by heat-induced epitope retrieval for 10 minutes at 95°C in citrate buffer, pH 6.0 (C9999; Sigma-Aldrich, Buchs, Switzerland). Nonspecific antibody binding was blocked at room

Figure 6. (See previous page). Loss of claudin-3 increases hepatic expression of the bile acid transporter *Ost1- β* . (A) Photographs of *Cldn3*^{+/+} and *Cldn3*^{-/-} gallbladders (n = 7). (B) RNA-seq data showing expression of bile transporters (n = 3, means \pm SD, **P* < .05, unpaired *t* test). (C) Comparative real-time qPCR determining the transcriptional levels of hepatic *Ost1- β* (*Slc51b*), *Asbt* (*Slc10a2*), and *Mdr3* (*Abcb4*) (n = 6, means \pm SD, **P* < .05, unpaired *t* test). (D) RNA-seq data showing hepatic expression of *Fxr* and its downstream targets (n = 3, means \pm SD, **P* < .05, unpaired *t* test). (E) Comparative real-time qPCR determining the transcriptional levels of *Fgf15* in the ileum (n = 5 for *Cldn3*^{+/+} and n = 9 for *Cldn3*^{-/-}, means \pm SD, unpaired *t* test). FXR, farnesoid X-receptor; NE, not expressed.



temperature for 1 hour using a protein-blocking solution (X0909; Dako, Santa Clara, CA). Antibodies were prepared in antibody diluent (S3022; Dako) at the following dilutions. Primary antibodies were as follows: Ki67 (RM-9106-S1, 1:300; Thermo Fisher Scientific, Basel, Switzerland); anti-phospho-histone H3 (06-570, 1:250; Merck Millipore, Burlington, MA); claudin-3 (NBP1-35668, 1:50; Novus Biologicals, Littleton, CO); and cytokeratin 7 (NBP1-88080, 1:200; Novus Biologicals). Secondary antibodies were as follows: anti-rabbit-Cy5 (A10523, 1:300; Fisher Scientific, Reinach, Switzerland); anti-mouse Alexa 488 (A-11001, 1:300; Fisher Scientific); and polyclonal rabbit anti-goat immunoglobulins/horseradish peroxidase (P0449; Dako). For the development of immunohistochemistry staining, streptavidin-peroxidase (71-00-38; BioConcept, Allschwil, Switzerland) and 3,3'-diaminobenzidine tetra hydrochloride (D4293-50SET; Sigma-Aldrich) were used. Primary antibodies were incubated with gentle agitation inside a wet chamber overnight at 4°C. Slides were washed for 20 minutes in PBS-Tween-20 (0.5%, P1379; Sigma-Aldrich) and incubated in darkness for 90 minutes with the secondary antibodies and 4',6-diamidino-2-phenylindole (DAPI) (D9542, diluted 1:2000; Sigma-Aldrich). After a final wash in PBS-Tween-20 (0.5%), slides were mounted with fluorescence mounting medium (H-1000; Vectorlabs, Burlingame, CA) and the coverslip was fixed with nail polish. For immunohistochemistry staining, erythrocytes were lysed in 5% H₂O₂ for 10 minutes before the first antibody incubation, and the staining was developed after the secondary antibody application by incubation with streptavidin-peroxidase for 30 minutes and 3,3'-diaminobenzidine tetra hydrochloride for 1 minute. Representative images that were selected for display in the publication were moderately adjusted in brightness and color intensity with the help of image editing software. Importantly, adjustments were always made in the same way for all samples.

For image acquisition, sections with 6- μ m or 10- μ m thickness were imaged using a fluorescent and bright-field microscope (panoramic 250 Flash III, panoramic scanner software, 3DHISTECH, Budapest, Hungary). Sections (30 μ m)

were imaged with a confocal microscope (LSM 710; Zeiss, Oberkochen, Germany), and 3-dimensional reconstructions from z-stack images were made using the Zeiss Zen software (Black edition, release version 8.1). Quantification of staining intensity and automated counting of Ki67-/pHH3-positive nuclei was performed exclusively on unmodified raw images.

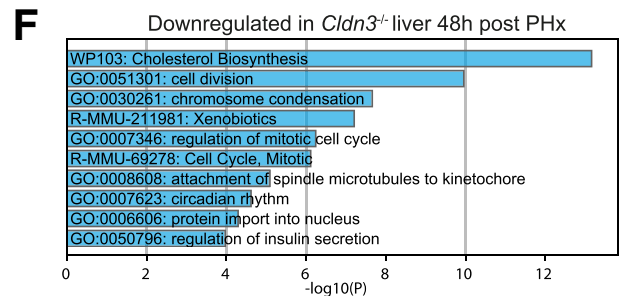
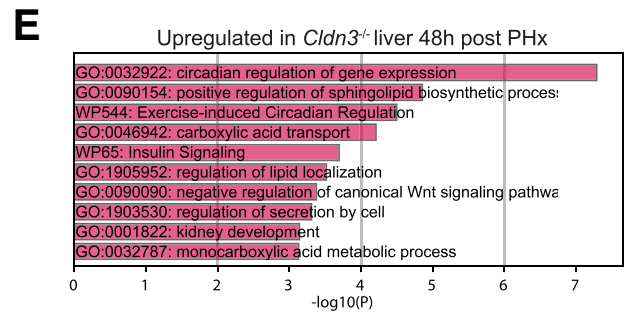
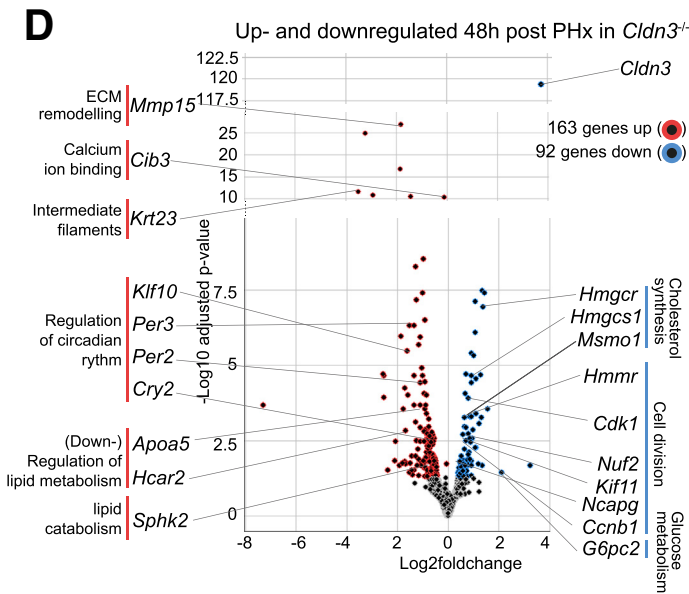
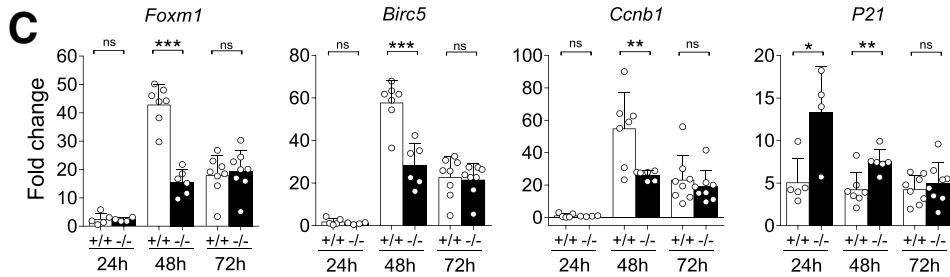
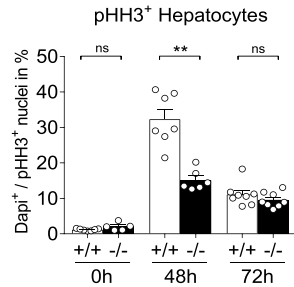
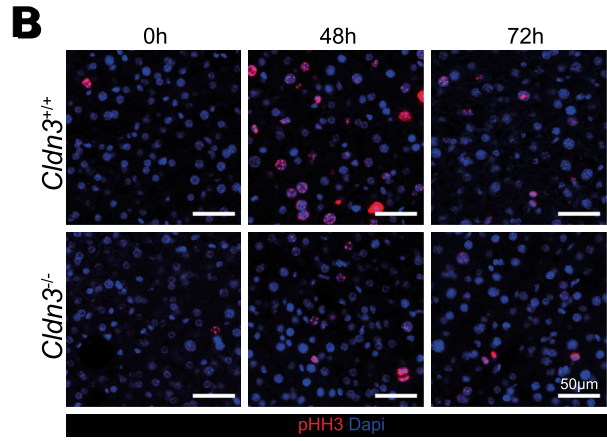
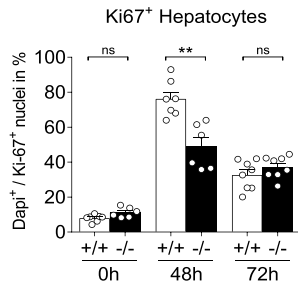
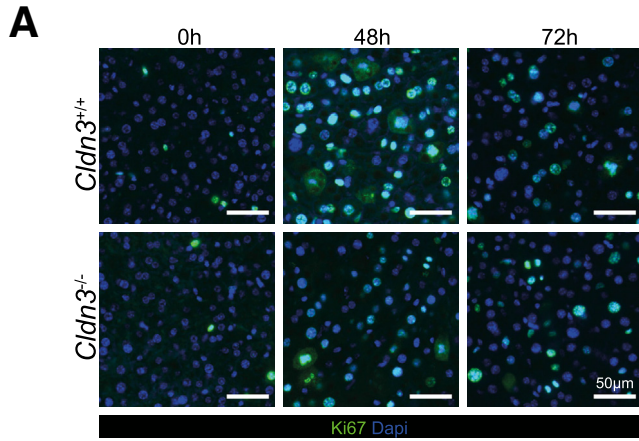
H&E staining. Liver paraffin sections were stained with hematoxylin (HX43078349; Merck) for 6 minutes and differentiated in hydrochloric acid : ethanol (1:1) performing 3 dips. Slides were incubated in eosin (45240; Fluka Chemical Corp, Charlotte, NC) for 3 minutes, followed by dehydration and mounting with Eukitt (Kindler, Freiburg im Breisgau, Germany).

Hepatic proliferation was quantified by imaging of 4 randomly chosen regions per liver, containing approximately 1000 DAPI-positive nuclei per region. Ki67- and pHH3-positive nuclei were counted and normalized as the percentage of all DAPI-positive cells with the help of ImageJ software (version 1.48; National Institutes of Health, Bethesda, MD).

Oil-red-O staining and quantification. Liver tissue was embedded in Tissue-Tek O.C.T. medium (4583; Sakura Finetek, Staufen im Breisgau, Germany), and 5- μ m cryosections were cut (CM3050S Cryostat; Leica, Wetzlar, Germany). Slides subsequently were stained with Oil-Red-O (O0625; Sigma-Aldrich): frozen sections were brought to room temperature, rinsed briefly in 60% triethyl phosphate (538728; Sigma-Aldrich), and subsequently stained in 0.5% Oil-red-O for 20 minutes. After a wash in distilled water, sections were counterstained in filtered hematoxylin (HX43078349; Merck, Dietikon, Germany) for 90 seconds, and nuclei were blued in saturated lithium carbonate (1.05680.0250; VWR, Dietikon, Switzerland) for 15 seconds. Slides then were rinsed with a flow of water for 5 minutes and mounted with glycerin jelly.

For staining quantification, a method based on previously published quantification techniques was used.^{69,70} The image analyzing software Fiji was used.⁷¹ Magnified images (40 \times) with areas of the exact same

Figure 7. (See previous page). *Cldn3* expression is regulated after PHx and claudin-3 loss does not induce inflammation in regenerating livers. Comparative real-time qPCR determining the transcriptional levels of *Cldn3* during a 7-day time course after PHx (n = 3, **P < .01, unpaired t test). (B) Anti-claudin-3 immunofluorescent stainings (green) in liver after PHx, and DAPI in blue. Representative images were taken. (C) Liver tissue Western blot for claudin-3 (20 kilodaltons) and β -actin (42 kilodaltons) at the indicated time points after PHx (n = 3/0–6 h, n = 4/0–24 h, n = 4/0–48 h). (D) Quantification of the Western blot in panel C. (E) Transmission electron microscopy images in liver tissue 6 hours after PHx. Arrowheads point to intact TJJs located at *Cldn3*^{+/+} and *Cldn3*^{-/-} bile canaliculi (BC). (F and G) Quantification of ductular reaction in liver tissue. Total liver protein was isolated 48 hours after PHx and used for anti-CK7 Western blot. Band intensities were normalized to β -actin. Expression of hepatic CK7 was similar in *Cldn3*^{+/+} and *Cldn3*^{-/-} mice (n = 5, unpaired t test, *Cldn3*^{+/+} band intensities were compared with their group average). (H) Serum cytokine levels 48 hours after PHx. With the exception of a slightly decreased MIP1 α concentration in *Cldn3*^{-/-} mice, there were no significant differences comparing the groups (n = 7 for *Cldn3*^{+/+} and n = 6 for *Cldn3*^{-/-}, means \pm SEM, *P < .05, unpaired t test). (I) Fluorescence-activated cell sorting analysis of hepatic immune cell frequencies at the indicated times after PHx. Despite a slightly higher B-cell frequency at 24 hours in *Cldn3*^{-/-} mice, there were no significant differences compared with *Cldn3*^{+/+} mice (at 0 h and 24 h: n = 5 for *Cldn3*^{+/+} and n = 4 for *Cldn3*^{-/-}; 48 h, n = 5; 72 h, n = 8; unpaired t test). Microscopes used for image acquisition in this figure were as follows: immune fluorescence, panoramic 250 Flash III, 3DHISTECH, panoramic scanner software, with a 20 \times objective; electron microscopy, Philips CM 12. CK7, cytokeratine 7; GM-CSF, granulocyte-macrophage colony-stimulating factor; IFN γ , interferon γ ; IL, interleukin; LIF, leukemia inhibitory factor; MIP1 α , macrophage inflammatory protein α ; NK, natural killer cells; NKT, natural killer T-cells; PC, pericentral; PP, periportal; TNF- α , tumor necrosis factor α .



sizes of 4 randomly chosen areas per sample were taken. Color deconvolution was performed (with the pre-set “H AEC”) to separate the hematoxylin and the Oil-red-O staining. The lipid droplet contained in the red channel was selected, and the threshold was adjusted to the same level for each image (values, 0 and 200). The threshold-adjusted image then was converted to a black-and-white 8-bit image (“apply”). The intensity of the staining then was measured with the analyze -> measure option. Staining intensities are given as integrated density.

Masson trichrome staining. Paraffin-embedded liver tissue was dewaxed and placed in Bouin’s fixative (HT10-1-32; Sigma-Aldrich) at 56°C for 10 minutes. After washing slides in tap water and distilled H₂O, slides were stained with hematoxylin (HT10-79; Sigma-Aldrich) for 5 minutes. After washing in running tap water and distilled H₂O, slides were destained once with HCl-alcohol (1:1) and rinsed again in distilled H₂O. Next, slides were put in Biebrich scarlet-scid fuchsin (HT151-250ML; Sigma-Aldrich) diluted 1:2 in 1% acetic acid (K45741563 425; Dr. Grogg Chemie, Stettlen, Switzerland) for 1 minute. Slides were rinsed and stained with phosphomolybdic-phosphotungstic acid (HT153-250ML and HT152-250ML; Sigma) 1:1 for 5 minutes. Slides then were stained with Aniline Blue (HT154-250ML; Sigma) for 20 minutes. After a last rinse, slides were put in 0.75% acetic acid, dehydrated, and mounted with Eukitt (Kindler).

Measurement of ALT, AST, and ALP in Serum

The liver injury markers ALT and AST were measured on the Cobas 8000 modular analyzer using the module C502 (Roche, Switzerland). ALP likewise was measured on the Cobas 8000, using the module C702 (Roche, Switzerland). All measurements were performed following the manufacturer’s instructions.

Electron Microscopy

Sample preparation and electron microscopy were performed as published previously.⁷² A variance in the cited protocol was used. In the lanthanide fixation step, samples were incubated in a water bath for 15 minutes at 50°C, without a prior incubation at room temperature. Transmission electron microscopy images were acquired using a Philips CM 12 microscope (Philips/Fei, Hillsboro, OR).

Flow Cytometry

Antibodies used for fluorescence-activated cell sorting can be found in Table 1. Livers were perfused with PBS via the portal vein until blanched and then put in Iscove’s modified Dulbecco’s medium (Gibco, Thermo Fisher Scientific, Waltham, MA), supplemented with 10% fetal bovine serum. Whole livers were passed through a metal spleen screen and digested with 0.05% collagenase IV (Worthington Biochemical) and DNase I (Sigma-Aldrich) for 30 minutes at 37°C. Intrahepatic mononuclear cells were purified on a Percoll gradient after centrifugation at 1250 × g for 20 minutes without braking. Cells subsequently were washed twice with PBS, and then resuspended in PBS containing 3% fetal bovine serum. Aliquots of 10⁶ cells/100 μL of staining buffer per well were incubated each with 1 μg of purified anti-CD16/CD32 for 20 minutes in the dark to block nonspecific binding of antibodies to the FcγIII- and II receptors (FcγIII- and II). Cell suspensions were incubated with cell viability dye eFluor 506 (Thermo Fisher Scientific) for 20 minutes at 4°C in the dark to exclude dead cells. Subsequently, these cells were stained separately with the following surface markers for 15 minutes with 1 μg of primary antibodies (Table 1). For cytokines and transcription factors, cells first were stained with antibodies to surface antigens, subsequently fixed, and permeabilized according to the manufacturer’s instructions (Foxp3/Transcription Factor Staining Buffer Set; eBioscience). Corresponding fluorochrome-labeled isotype control antibodies were used for staining controls. Cells resuspended in 250 μL of buffer (0.15 mol/L NaCl, 1 mmol/L NaH₂PO₄ H₂O, 10 mmol/L Na₂HPO₄ 2H₂O, and 3 mmol/L NaN₃) were analyzed in a flow cytometer (BD LSR II; BD Pharmingen, Inc, San Diego, CA) using the corresponding BD FACSDiva software. Flow cytometric analysis was performed using FlowJo software (Treestar, Inc, Ashland, OR).

Western Blot

Total protein was extracted from liver tissue or cultured cells using RIPA lysis buffer and a TissueLysor II (Qiagen, Hilden, Germany). Lysates were centrifuged for 15 minutes at 20,000 × g, and the supernatant was aliquoted. Protein concentrations were quantified by Bradford assay (5000006; Bio-Rad, Cressier, Switzerland) and a microplate reader. Precast gels (456-1094; Bio-Rad) were used to separate equalized amounts of protein per sample by

Figure 8. (See previous page). Claudin-3 contributes to optimal liver regeneration. (A and B) Immunofluorescent staining of anti-Ki67 (green) or anti-pHH3 (red) in liver tissue after PHx, comparing *Cldn3*^{+/+} and *Cldn3*^{-/-} livers. DAPI in blue. Quantification of the proliferation scores below (0 h and 48 h: n = 7 for *Cldn3*^{+/+} and n = 6 for *Cldn3*^{-/-}; 72 h: n = 8, bars represent the means ± SEM, **P < .01, unpaired t test). Representative images were taken. (C) Comparative real-time qPCR determining the cell-cycle-related gene expression after PHx (24 h: n = 5 for *Cldn3*^{+/+} and n = 4 for *Cldn3*^{-/-}; 48 h: n = 7 for *Cldn3*^{+/+} and n = 6 for *Cldn3*^{-/-}; 72 h: n = 8, bars represent means ± SEM, *P < .05, **P < .01, ***P < .001, unpaired t test). (D) Volcano plot showing up-regulated and down-regulated genes (red circles and blue circles, respectively) in *Cldn3*^{-/-} compared with *Cldn3*^{+/+} liver tissue at 48 hours after PHx. RNA-seq analysis is performed by DESeq2 (n = 3, differential expression significance threshold: P value adjusted < .05). Genes with low expression in *Cldn3*^{-/-} are shown in blue, and with high expression in red circles. A selection of significantly regulated genes that were identified with Metascape analysis are annotated. Metascape analysis of the (E) top 10 up-regulated and (F) top 10 down-regulated gene pathways within the data set of panel D. Microscopes used for image acquisition in this figure were as follows: panoramic 250 Flash III, 3DHISTECH, panoramic scanner software, with a 20× objective. ECM, extracellular matrix.

Table 1. Antibodies Used for Fluorescence-Activated Cell Sorting

Fluorescence	Cell marker	Clone	Company	Catalog no.
Alexa Fluor 700	NK1.1	PK136	BioLegend (San Diego, CA)	108730
PE-cy5	NK1.1	PK136	BioLegend	108716
PE-efluor-610	Eomes	Dan11mag	eBioscience (San Diego, CA)	61-4875-82
APC	Roryt	AFKJS-9	eBioscience	17-6988-80
APC-efluor780	PD-1	J43	eBioscience	47-9985-82
eFluor450	PD-1	J43	eBioscience	48-9985-82
PE	IL-22	Poly5164	BioLegend	516404
Percp-efluor710	IL-22	1H8PWSR	eBioscience	46-7221-80
PE-cy7	CD49b	DX5	BioLegend	108922
PE-cy7	CD4	GK1.5	eBioscience	25-0041-81
APC	CD4	RM4-4	BioLegend	116014
BV570	CD8	53-6.7	BioLegend	301038
Alexa Fluor 700	CD11b	M1/70	BioLegend	101222
BV421	CD49a	Ha31/8	BD Biosciences (Allschwil, Switzerland)	740046
APC-efluor780	INF- γ	XMG1.2	eBioscience	47-7311-82
FITC	INF- γ	XMG1.2	BioLegend	505806
PE	INF- γ	XMG1.2	eBioscience	12-7311-41
PE	CD19	SJ25C1	eBioscience	12-0198-41
PE-Dazzle 594	CD19	6D5	BioLegend	115554
BUV395	CD45	30-F11(Ruo)	BD Biosciences	564279
Percp cy.5.5	FoxP3	FJK-16s	eBioscience	45-5773-80
PE	FoxP3	FJK-16s	eBioscience	12-5773-80
PE-Dazzle 594	CD152	UC10-4B9	BioLegend	106318
APC	IL-10	JES5-16E3	BioLegend	505010
PE	IL-10	JES3-9D7	eBioscience	12-7108-41
FITC	CD69	H1.2F3	BioLegend	104506
PE	Ly6G	RB6-8C5	eBioscience	12-8931-81
PE-cy7	Ly6G	RB6-8C5	eBioscience	25-5931-81
APC	F4/80	BM8	eBioscience	17-4801-82
eFluor450	CD11c	N418	eBioscience	48-0114-82
FITC	TNF α	MP6-XT22	BioLegend	506304
eFluor506	Viability dye	-	eBioscience	65-0866-18
-	CD16/CD32	2.4 G2	BioLegend	101302

sodium dodecyl sulfate–polyacrylamide gel electrophoresis, under reducing conditions. Proteins then were transferred on nitrocellulose membranes (170-4158; Bio-Rad). Membranes were blocked with 5% w/v nonfat dry milk in PBS for 1 hour at room temperature. Primary antibodies were diluted in the blocking medium and incubated overnight at 4°C. Primary antibodies were as follows: claudin-3 (NBP1-35668, 1:500–1:1000; Novus Biologicals); cytokeratin 7 (NBP1-88080, 1:200; Novus Biologicals); and anti- β -actin–peroxidase (A3854, 1:50,000; Sigma-Aldrich); the secondary antibody used was anti-rabbit–horseradish peroxidase (P0448, 1:2000; Dako).

After primary antibody incubation, membranes were washed 3 times for 5 minutes in PBS–Tween-20 (0.1%). Secondary antibodies were diluted with 5% w/v nonfat dry milk in PBS, and the membranes were incubated for 1 hour at room temperature, followed by 3 washing steps for 30 minutes in total. Enhanced chemiluminescence solution

(NEL105001EA; PerkinElmer, Waltham, MA) was added for 1 minute to develop the signal. Films in combination with a developer (AGFA, CURIX 60, Mortsel, Belgium) were used to visualize the bands. The correct band size was estimated with the help of a standard protein ladder (161-0374; Bio-Rad).

Real-Time qPCR mRNA Expression Analysis

RNA from snap-frozen tissue has been extracted using NucleoZOL (740404.200; Macherey-Nagel, Düren, Germany). Complementary DNA was made from 500 ng of tissue RNA using the Omniscript reverse-transcriptase kit (205113; Qiagen). Per reaction, 11.25 ng complementary DNA was used. Real-time qPCRs have been performed on an ABI 7500 thermocycler (Applied Biosystems, Foster City, CA) using TaqMan and on an ABI 7900 HT thermocycler (Applied Biosystems) for the SYBR green–based assays. The corresponding reaction mixtures

(TaqMan, 4914058001 and SYBR green, 000000004913914001; both Sigma-Aldrich) were used. Cycling conditions were chosen according to the vendor instructions of the DNA polymerase master mixes. TaqMan real-time qPCR primers used were as follows: *Ccnb1* (Mm03053893_gH; Thermo Fisher Scientific), *Birc5* (Mm00599749_m1; Thermo Fisher Scientific), *Foxm1* (Mm00514924_m1; Thermo Fisher Scientific), *Cdkn1a* (p21) (Mm00432448_m1; Thermo Fisher Scientific), *Tbp* (Mm00446971-m1; Thermo Fisher Scientific), *Mdr3* (4448892; Thermo Fisher Scientific), *Ost1- β* (Mm01175040_m1; Thermo Fisher Scientific), and *Asbt* (Mm00488258_m1; Thermo Fisher Scientific). SYBR real-time qPCR primers used were as follows: *Cldn3* forward: GCACCCACCAAGATCCTCTA, *Cldn3* reverse: TCGTCTGTACCATCTGGAA (*Cldn3* SYBR primer has been published⁷³), *Fgf15* forward: CCAACTGCTTCCTCCGAATCC, *Fgf15* reverse: TACAGTCTTCTCCGAGTAGC, *Eef1a1* forward: CGTTCTTTTTTCGCAACGGGT, *Eef1a1* reverse: TTGCCGGAATCTACGTGTCC (designed with NCBI Primer-BLAST, Bethesda, MD). Fold- and log₂-fold changes in gene expression were calculated using the delta-delta CT method.

RNA Sequencing

Total RNA was extracted from the liver with NucleoZOL (740404.200; Macherey-Nagel), and quantified by a bio-analyzer (Bio-Rad). Sequencing was prepared with paired-end reads of 50 bp, TruSeq Stranded mRNA (Illumina, San Diego, CA). Sequencing was performed on a NovaSeq6000 (Illumina).

RNA-seq alignment. Fastq files were aligned to the mouse reference genome mm10 ENSEMBL (European Molecular Biology Laboratory's European Bioinformatics Institute, Hinxton, Cambridge, UK) release 102⁷⁴ with hisat2 v. 2.2.1,⁷⁵ and transformed into bam files with SAMtools v. 1.10.⁷⁶ The read count matrix was produced from the bam files via featureCount shell version 2.0.1.⁷⁷

Dimensionality reduction. For the principal component analysis, the read count matrix was variance-stabilizing-transformed using `vst()`, then principal components were computed and visualized using `plotPCA()` functions from the DESeq2 R package,⁷⁸ with default parameters.

RNA-seq differential expression. Differentially expressed genes were computed with R package DESeq2. Two technical replicates of control sample 5 were analyzed together by collapsing them using the DESeq2 `collapseReplicates` function. Genes with a *P* value less than .05 adjusted by false discovery rate were considered statistically significant for further analysis. For volcano plot visualization, log₂-fold changes obtained from DESeq2 analysis were shrunk using the `apeglm` shrinkage estimator.⁷⁹

Enrichment analysis. Metascape⁸⁰ was used to determine the pathways to which genes were associated.

Oral Glucose Tolerance Test, Glucose, and Insulin Measurements

Before the oral glucose tolerance test, mice were fasted overnight (16 hours), followed by baseline blood glucose and insulin levels measurements. A bodyweight-adjusted

amount of glucose was given by oral gavage (2 mg/g bodyweight). Glucose and insulin levels subsequently were determined. Blood for glucose was obtained by blood collection from the left and right saphenous vein (<1 μ L). Blood/serum for insulin measurements was obtained by exsanguination (under anesthesia) via cardiac puncture. Glucose levels were determined with the use of a commercial glucometer (Accu-chek Aviva; Hoffmann-La Roche, Basel, Switzerland). Serum insulin levels were determined with the Ultra-Sensitive Mouse Insulin ELISA Kit (90080; Crystal Chem, Elk Grove Village, IL), according to the manufacturer's instructions.

Bile Acid Quantification

The method applied was described recently.^{81,82} Briefly, for quantification of bile acids, 25- μ L serum samples diluted 1:4 with water, and calibrators, were subjected to protein precipitation by adding 900 μ L of 2-propanol and a mixture of deuterated internal standards. Extraction was performed for 30 minutes at 4°C with continuous shaking, followed by centrifuging at 16,000 \times g for 10 minutes. Supernatants were transferred to new tubes, evaporated to dryness, and reconstituted with 100 μ L methanol:water (1:1, v/v). For the extraction of liver samples, 900 μ L of chloroform:methanol:water (1:3:1, v/v/v) and 100 μ L internal standard mixture were added to a Precellys tube (VWR, Radnor, PA) containing beads and 30 \pm 5 mg of liver tissue. Samples were homogenized with a Precellys tissue homogenizer, and centrifuged at 16,000 \times g for 10 minutes at 20°C. The supernatant was transferred to a new tube and the procedure was repeated by adding 800 μ L extraction solvent. After evaporation to dryness, samples were resuspended with 200 μ L methanol:water (1:1, v/v). The injection volume in both cases was 3 μ L. Liquid chromatography-tandem mass spectrometry consisted of an Agilent 1290 ultra performance liquid chromatography coupled to an Agilent 6490 triple quadrupole mass spectrometer equipped with an electrospray ionization source (Agilent Technologies, Basel, Switzerland). Chromatographic separation of bile acids was achieved using a reversed-phase column (Acquity UPLC BEH C18, 1.7 mm, 2.1 μ m, 150 mm; Waters, Wexford, Ireland).⁸²

Measurement of Serum Proinflammatory Cytokines

Serum cytokines were determined on a cytokine array. The array was performed by Eve technologies (Calgary, Canada), using the following application: Chemokine Array 31-Plex (MD31), based on Millipore Milliplex (Merck, Darmstadt, Germany).

Statistical Tests Used to Analyze Data

The statistical tests used to analyze the data are fitted for each experiment and are described within each figure legend.

All authors had access to the study data and have reviewed and approved the final manuscript.

References

- Zihni C, Mills C, Matter K, Balda MS. Tight junctions: from simple barriers to multifunctional molecular gates. *Nat Rev Mol Cell Biol* 2016;17:564–580.
- Hwang I, Yang H, Kang H-S, Ahn C-H, Lee G-S, Hong E-J, An B-S, Jeung E-B. Spatial expression of claudin family members in various organs of mice. *Mol Med Rep* 2014;9:1806–1812.
- Hwang I, An BS, Yang H, Kang HS, Jung EM, Jeung EB. Tissue-specific expression of occludin, zona occludens-1, and junction adhesion molecule A in the duodenum, ileum, colon, kidney, liver, lung, brain, and skeletal muscle of C57BL mice. *J Physiol Pharmacol* 2013;64:11–18.
- Pradhan-Sundd T, Monga SP. Blood-bile barrier: morphology, regulation, and pathophysiology. *Gene Expression* 2019;19:69–87.
- Ding L, Lu Z, Lu Q, Chen Y-H. The claudin family of proteins in human malignancy: a clinical perspective. *Cancer Manag Res* 2013;5:367–375.
- Günzel D, Yu ASL. Claudins and the modulation of tight junction permeability. *Physiol Rev* 2013;93:525–569.
- Colegio OR, Van Itallie CM, McCrea HJ, Rahner C, Anderson JM. Claudins create charge-selective channels in the paracellular pathway between epithelial cells. *Am J Physiol Cell Physiol* 2002;283:C142–C147.
- Tabariès S, Siegel PM. The role of claudins in cancer metastasis. *Oncogene* 2017;36:1176–1190.
- Lal-Nag M, Morin PJ. The claudins. *Genome Biol* 2009;10:235.
- Evans MJ, von Hahn T, Tscherne DM, Syder AJ, Panis M, Wölk B, Hatzioannou T, McKeating JA, Bieniasz PD, Rice CM. Claudin-1 is a hepatitis C virus co-receptor required for a late step in entry. *Nature* 2007;446:801–805.
- Benedicto I, Molina-Jimenez F, Bartosch B, Cosset F-L, Lavillette D, Prieto J, Moreno-Otero R, Valenzuela-Fernandez A, Aldabe R, Lopez-Cabrera M, Majano PL. The tight junction-associated protein occludin is required for a postbinding step in hepatitis C virus entry and infection. *J Virol* 2009;83:8012–8020.
- Meertens L, Bertaux C, Cukierman L, Cormier E, Lavillette D, Cosset F-L, Dragic T. The tight junction proteins claudin-1, -6, and -9 are entry cofactors for hepatitis C virus. *J Virol* 2008;82:3555–3560.
- Fujita K, Katahira J, Horiguchi Y, Sonoda N, Furuse M, Tsukita S. Clostridium perfringens enterotoxin binds to the second extracellular loop of claudin-3, a tight junction integral membrane protein. *FEBS Lett* 2000;476:258–261.
- Roehlen N, Roca Suarez AA, El Saghire H, Saviano A, Schuster C, Lupberger J, Baumert TF. Tight junction proteins and the biology of hepatobiliary disease. *Int J Mol Sci* 2020;21:825.
- Tanaka H, Yamamoto Y, Kashihara H, Yamazaki Y, Tani K, Fujiyoshi Y, Mineta K, Takeuchi K, Tamura A, Tsukita S. Claudin-21 has a paracellular channel role at tight junctions. *Mol Cell Biol* 2016;36:954–964.
- Hadj-Rabia S, Baala L, Vabres P, Hamel-Teillac D, Jacquemin E, Fabre M, Lyonnet S, de Prost Y, Munnich A, Hadchouel M, Smahi A. Claudin-1 gene mutations in neonatal sclerosing cholangitis associated with ichthyosis: a tight junction disease. *Gastroenterology* 2004;127:1386–1390.
- Baala L, Hadj-Rabia S, Hamel-Teillac D, Hadchouel M, Prost C, Leal SM, Jacquemin E, Sefiani A, de Prost Y, Courtois G, Munnich A, Lyonnet S, Vabres P. Homozygosity mapping of a locus for a novel syndromic ichthyosis to chromosome 3q27–q28. *J Invest Dermatol* 2002;119:70–76.
- Matsumoto K, Yamazaki Y, Tanaka H, Watanabe M, Eguchi H, Nagano H, Hikita H, Tatsumi T, Takehara T, Tamura A, Tsukita S. Claudin 2 deficiency reduces bile flow and increases susceptibility to cholesterol gallstone disease in mice. *Gastroenterology* 2014;147:1134–1145.e10.
- Bouchagier KA, Assimakopoulos SF, Karavias DD, Maroulis I, Tzelepi V, Kalofonos H, Karavias DD, Kardamakis D, Scopa CD, Tsamandas AC. Expression of claudins-1, -4, -5, -7 and occludin in hepatocellular carcinoma and their relation with classic clinicopathological features and patients' survival. *In Vivo* 2014;28:315–326.
- Milatz S, Krug SM, Rosenthal R, Günzel D, Müller D, Schulzke J-D, Amasheh S, Fromm M. Claudin-3 acts as a sealing component of the tight junction for ions of either charge and uncharged solutes. *Biochim Biophys Acta* 2010;1798:2048–2057.
- Rahner C, Mitic LL, Anderson JM. Heterogeneity in expression and subcellular localization of claudins 2, 3, 4, and 5 in the rat liver, pancreas, and gut. *Gastroenterology* 2001;120:411–422.
- Tanaka H, Imasato M, Yamazaki Y, Matsumoto K, Kunimoto K, Delpierre J, Meyer K, Zerial M, Kitamura N, Watanabe M, Tamura A, Tsukita S. Claudin-3 regulates bile canalicular paracellular barrier and cholesterol gallstone core formation in mice. *J Hepatol* 2018;69:1308–1316.
- Garcia-Hernandez V, Quiros M, Nusrat A. Intestinal epithelial claudins: expression and regulation in homeostasis and inflammation: intestinal epithelial claudins. *Ann N Y Acad Sci* 2017;1397:66–79.
- Ahmad R, Rah B, Bastola D, Dhawan P, Singh AB. Obesity-induces organ and tissue specific tight junction restructuring and barrier deregulation by claudin switching. *Sci Rep* 2017;7:5125.
- Patel RM, Myers LS, Kurundkar AR, Maheshwari A, Nusrat A, Lin PW. Probiotic bacteria induce maturation of intestinal claudin 3 expression and barrier function. *Am J Pathol* 2012;180:626–635.
- Sanchez-Taltavull D, Perkins TJ, Dommann N, Melin N, Keogh A, Candinas D, Stroka D, Beldi G. Bayesian correlation is a robust gene similarity measure for single-cell RNA-seq data. *NAR Genom Bioinform* 2020;2:lqaa002.
- Castro Dias M, Coisne C, Lazarevic I, Baden P, Hata M, Iwamoto N, Francisco DMF, Vanlandewijck M, He L, Baier FA, Stroka D, Bruggmann R, Lyck R, Enzmann G, Deutsch U, Betsholtz C, Furuse M, Tsukita S, Engelhardt B. Claudin-3-deficient C57BL/6J mice display intact brain barriers. *Sci Rep* 2019;9:203.

28. Fickert P, Wagner M. Biliary bile acids in hepatobiliary injury – what is the link? *J Hepatol* 2017;67:619–631.
29. Woo S-L, Guo T, Wu C. Hepatic lipogenesis: nutritional control and pathophysiological relevance. In: Ntambi JM, ed. *Hepatic de novo lipogenesis and regulation of metabolism*. Cham, Basel, Switzerland: Springer International Publishing, 2016:211–234.
30. Ogrodnik M, Miwa S, Tchkonina T, Tiniakos D, Wilson CL, Lahat A, Day CP, Burt A, Palmer A, Anstee QM, Grellscheid SN, Hoeijmakers JHJ, Barnhoorn S, Mann DA, Bird TG, Vermeij WP, Kirkland JL, Passos JF, von Zglinicki T, Jurk D. Cellular senescence drives age-dependent hepatic steatosis. *Nat Commun* 2017; 8:15691.
31. Luo D, Li J, Chen K, Yin Y, Fang Z, Pang H, Rong X, Guo J. Study on metabolic trajectory of liver aging and the effect of Fufang Zhenzhu Tiaozhi on aging mice. *Front Pharmacol* 2019;10:926.
32. Hunt NJ, Kang SW, Lockwood GP, Le Couteur DG, Cogger VC. Hallmarks of aging in the liver. *Comput Struct Biotechnol J* 2019;17:1151–1161.
33. Fiorucci S, Biagioli M, Zampella A, Distrutti E. Bile acids activated receptors regulate innate immunity. *Front Immunol* 2018;9:1853.
34. Sato Y, Koyama S, Tsukada K, Hatakeyama K. Acute portal hypertension reflecting shear stress as a trigger of liver regeneration following partial hepatectomy. *Surg Today* 1997;27:518–526.
35. Takakuwa Y, Kokai Y, Sasaki K, Chiba H, Tobioka H, Mori M, Sawada N. Bile canalicular barrier function and expression of tight-junctional molecules in rat hepatocytes during common bile duct ligation. *Cell Tissue Res* 2002;307:181–189.
36. Kojima T. Tight junction proteins and signal transduction pathways in hepatocytes. *Histol Histopathol* 2009; 11:1463–1472.
37. Sakaguchi T, Suzuki S, Higashi H, Inaba K, Nakamura S, Baba S, Kato T, Konno H. Expression of tight junction protein claudin-5 in tumor vessels and sinusoidal endothelium in patients with hepatocellular carcinoma. *J Surg Res* 2008;147:123–131.
38. D'Agnillo F, Williams MC, Moayeri M, Warfel JM. Anthrax lethal toxin downregulates claudin-5 expression in human endothelial tight junctions. *PLoS One* 2013;8:e62576.
39. Holczbauer Á, Gyöngyösi B, Lotz G, Törzsök P, Kaposi-Novák P, Szijártó A, Tátrai P, Kupcsulik P, Schaff Z, Kiss A. Increased expression of claudin-1 and claudin-7 in liver cirrhosis and hepatocellular carcinoma. *Pathol Oncol Res* 2014;20:493–502.
40. Inai T, Sengoku A, Guan X, Hirose E, Iida H, Shibata Y. Heterogeneity in expression and subcellular localization of tight junction proteins, claudin-10 and -15, examined by RT-PCR and immunofluorescence microscopy. *Arch Histol Cytol* 2005;68:349–360.
41. Morita K, Furuse M, Fujimoto K, Tsukita S. Claudin multigene family encoding four-transmembrane domain protein components of tight junction strands. *Proc Natl Acad Sci U S A* 1999;96:511–516.
42. D'Souza T, Sherman-Baust CA, Poosala S, Mullin JM, Morin PJ. Age-related changes of claudin expression in mouse liver, kidney, and pancreas. *J Gerontology A Biol Sci Med Sci* 2009;64A:1146–1153.
43. Gebhardt R, Matz-Soja M. Liver zonation: novel aspects of its regulation and its impact on homeostasis. *World J Gastroenterol* 2014;20:8491–8504.
44. Kietzmann T. Metabolic zonation of the liver: the oxygen gradient revisited. *Redox Biol* 2017;11:622–630.
45. Halpern KB, Shenhav R, Matcovitch-Natan O, Toth B, Lemze D, Golan M, Massasa EE, Baydatch S, Landen S, Moor AE, Brandis A, Giladi A, Avihail AS, David E, Amit I, Itzkovitz S. Single-cell spatial reconstruction reveals global division of labour in the mammalian liver. *Nature* 2017;542:352–356.
46. Macpherson AJ, Heikenwalder M, Ganai-Vonarburg SC. The liver at the nexus of host-microbial interactions. *Cell Host Microbe* 2016;20:561–571.
47. Shao W, Espenshade PJ. Expanding roles for SREBP in metabolism. *Cell Metab* 2012;16:414–419.
48. Meng Z, Liu N, Fu X, Wang X, Wang Y, Chen W, Zhang L, Forman BM, Huang W. Insufficient bile acid signaling impairs liver repair in CYP27^{-/-} mice. *J Hepatol* 2011; 55:885–895.
49. Pratt-Hyatt M, Lickteig AJ, Klaassen CD. Tissue distribution, ontogeny, and chemical induction of aldo-keto reductases in mice. *Drug Metab Dispos* 2013; 41:1480–1487.
50. Herrema H, Meissner M, van Dijk TH, Brufau G, Boverhof R, Oosterveer MH, Reijngoud D-J, Müller M, Stellaard F, Groen AK, Kuipers F. Bile salt sequestration induces hepatic de novo lipogenesis through farnesoid X receptor- and liver X receptor α -controlled metabolic pathways in mice. *Hepatology* 2010;51:806–816.
51. Nikolaou N, Gathercole LL, Marchand L, Althari S, Dempster NJ, Green CJ, van de Bunt M, McNeil C, Arvaniti A, Hughes BA, Sgromo B, Gillies RS, Marschall H-U, Penning TM, Ryan J, Artl W, Hodson L, Tomlinson JW. AKR1D1 is a novel regulator of metabolic phenotype in human hepatocytes and is dysregulated in non-alcoholic fatty liver disease. *Metabolism* 2019; 99:67–80.
52. Thekkinghat AA, Yadav KK, Rangarajan PN. Apolipoprotein L9 interacts with LC3/GABARAP and is a microtubule-associated protein with a widespread subcellular distribution. *Biol Open* 2019;8:bio045930.
53. Snyder JM, Zhong G, Hogarth C, Huang W, Topping T, LaFrance J, Palau L, Czuba LC, Griswold M, Ghiaur G, Isoherranen N. Knockout of Cyp26a1 and Cyp26b1 during postnatal life causes reduced lifespan, dermatitis, splenomegaly, and systemic inflammation in mice. *FASEB J* 2020;34:15788–15804.
54. Pavlović N, Goločorbin-Kon S, Đanić M, Stanimirov B, Al-Salami H, Stankov K, Mikov M. Bile acids and their derivatives as potential modifiers of drug release and pharmacokinetic profiles. *Front Pharmacol* 2018;9:1283.
55. Zou Y, Bao Q, Kumar S, Hu M, Wang G-Y, Dai G. Four waves of hepatocyte proliferation linked with three waves of hepatic fat accumulation during partial hepatectomy-induced liver regeneration. *PLoS One* 2012;7:e30675.
56. Brasaemle DL. Cell biology: enhanced: a metabolic push to proliferate. *Science* 2006;313:1581–1582.

57. Huang W. Nuclear receptor-dependent bile acid signaling is required for normal liver regeneration. *Science* 2006;312:233–236.
58. Takaki Y, Hirai S, Manabe N, Izumi Y, Hirose T, Nakaya M, Suzuki A, Mizuno K, Akimoto K, Tsukita S, Shuin T, Ohno S. Dynamic changes in protein components of the tight junction during liver regeneration. *Cell Tissue Res* 2001;305:399–409.
59. Naugler WE. Bile acid flux is necessary for normal liver regeneration. *PLoS One* 2014;9:e97426.
60. Uriarte I, Fernandez-Barrena MG, Monte MJ, Latasa MU, Chang HCY, Carotti S, Vespasiani-Gentilucci U, Morini S, Vicente E, Concepcion AR, Medina JF, Marin JJG, Berasain C, Prieto J, Avila MA. Identification of fibroblast growth factor 15 as a novel mediator of liver regeneration and its application in the prevention of post-resection liver failure in mice. *Gut* 2013;62:899–910.
61. Pereyra D, Starlinger P. Shaping the future of liver surgery: Implementation of experimental insights into liver regeneration. *Eur Surg* 2018;50:132–136.
62. Ahmed N, Vernick JJ. Management of liver trauma in adults. *J Emerg Trauma Shock* 2011;4:114–119.
63. Zhang P, Wang S, Wang S, Qiao J, Zhang L, Zhang Z, Chen Z. Dual function of partitioning-defective 3 in the regulation of YAP phosphorylation and activation. *Cell Discovery* 2016;2:16021.
64. Sourisseau T, Georgiadis A, Tsapara A, Ali RR, Pestell R, Matter K, Balda MS. Regulation of PCNA and cyclin D1 expression and epithelial morphogenesis by the ZO-1-regulated transcription factor ZONAB/DbpA. *Mol Cell Biol* 2006;26:2387–2398.
65. Huerta M, Muñoz R, Tapia R, Soto-Reyes E, Ramírez L, Recillas-Targa F, González-Mariscal L, López-Bayghen E. Cyclin D1 is transcriptionally down-regulated by ZO-2 via an E box and the transcription factor c-Myc. *Mol Biol Cell* 2007;18:4826–4836.
66. Nava P, Capaldo CT, Koch S, Kolegraff K, Rankin CR, Farkas AE, Feasel ME, Li L, Addis C, Parkos CA, Nusrat A. JAM-A regulates epithelial proliferation through Akt/ β -catenin signalling. *EMBO Rep* 2011;12:314–320.
67. Loforese G, Malinka T, Keogh A, Baier F, Simillion C, Montani M, Halazonetis TD, Candinas D, Stroka D. Impaired liver regeneration in aged mice can be rescued by silencing Hippo core kinases MST1 and MST2. *EMBO Mol Med* 2017;9:46–60.
68. van Dijk D, Sharma R, Nainys J, Yim K, Kathail P, Carr AJ, Burdziak C, Moon KR, Chaffer CL, Pattabiraman D, Bierende B, Mazutis L, Wolf G, Krishnaswamy S, Pe'er D. Recovering gene interactions from single-cell data using data diffusion. *Cell* 2018;174:716–729.e27.
69. Deutsch MJ, Schriever SC, Roscher AA, Ensenauer R. Digital image analysis approach for lipid droplet size quantitation of Oil Red O-stained cultured cells. *Anal Biochem* 2014;445:87–89.
70. Febres-Aldana CA, Alghamdi S, Krishnamurthy K, Poppiti RJ. Liver fibrosis helps to distinguish autoimmune hepatitis from DILI with autoimmune features: a review of twenty cases. *J Clin Transl Hepatol* 2019;7:21–26.
71. Schindelin J, Arganda-Carreras I, Frise E, Kaynig V, Longair M, Pietzsch T, Preibisch S, Rueden C, Saalfeld S, Schmid B, Tinevez J-Y, White DJ, Hartenstein V, Eliceiri K, Tomancak P, Cardona A. Fiji: an open-source platform for biological-image analysis. *Nat Methods* 2012;9:676–682.
72. Odriozola A, Llodrá J, Radecke J, Rueggsegger C, Tschanz S, Saxena S, Rohr S, Zuber B. High contrast staining for serial block face scanning electron microscopy without uranyl acetate. *bioRxiv*. <https://doi.org/10.1101/207472>.
73. Chihara M, Ikebuchi R, Otsuka S, Ichii O, Hashimoto Y, Suzuki A, Saga Y, Kon Y. Mice stage-specific claudin 3 expression regulates progression of meiosis in early stage spermatocytes. *Biol Reprod* 2013;89:3.
74. Yates AD, Achuthan P, Akanni W, Allen J, Allen J, Alvarez-Jarreta J, Amode MR, Armean IM, Azov AG, Bennett R, Bhai J, Billis K, Boddu S, Marugán JC, Cummins C, Davidson C, Dodiya K, Fatima R, Gall A, Giron CG, Gil L, Grego T, Haggerty L, Haskell E, Hourlier T, Izuogu OG, Janacek SH, Juettemann T, Kay M, Lavidas I, Le T, Lemos D, Martinez JG, Maurel T, McDowall M, McMahon A, Mohanan S, Moore B, Nuhn M, Oheh DN, Parker A, Parton A, Patricio M, Sakthivel MP, Abdul Salam AI, Schmitt BM, Schuilenburg H, Sheppard D, Sycheva M, Szuba M, Taylor K, Thormann A, Threadgold G, Vullo A, Walts B, Winterbottom A, Zadissa A, Chakiachvili M, Flint B, Frankish A, Hunt SE, Ilesley G, Kostadima M, Langridge N, Loveland JE, Martin FJ, Morales J, Mudge JM, Muffato M, Perry E, Ruffier M, Trevanion SJ, Cunningham F, Howe KL, Zerbino DR, Flicek P. Ensembl 2020. *Nucleic Acids Res* 2020;48:D682–D688.
75. Kim D, Paggi JM, Park C, Bennett C, Salzberg SL. Graph-based genome alignment and genotyping with HISAT2 and HISAT-genotype. *Nat Biotechnol* 2019;37:907–915.
76. Li H, Handsaker B, Wysoker A, Fennell T, Ruan J, Homer N, Marth G, Abecasis G, Durbin R. The sequence alignment/Map format and SAMtools. *Bioinformatics* 2009;25:2078–2079.
77. Liao Y, Smyth GK, Shi W. FeatureCounts: an efficient general purpose program for assigning sequence reads to genomic features. *Bioinformatics* 2014;30:923–930.
78. Love MI, Huber W, Anders S. Moderated estimation of fold change and dispersion for RNA-seq data with DESeq2. *Genome Biol* 2014;15:550.
79. Zhu A, Ibrahim JG, Love MI. Heavy-tailed prior distributions for sequence count data: removing the noise and preserving large differences. *Bioinformatics* 2019;35:2084–2092.
80. Zhou Y, Zhou B, Pache L, Chang M, Khodabakhshi AH, Tanaseichuk O, Benner C, Chanda SK. Metascape provides a biologist-oriented resource for the analysis of systems-level datasets. *Nat Commun* 2019;10:1523.
81. Gómez C, Stücheli S, Kratschmar DV, Bouitbir J, Odermatt A. Development and validation of a highly sensitive LC-MS/MS method for the analysis of bile acids in serum, plasma, and liver tissue samples. *Metabolites* 2020;10:282.

82. Penno CA, Arsenijevic D, Da Cunha T, Kullak-Ublick GA, Montani J-P, Odermatt A. Quantification of multiple bile acids in uninephrectomized rats using ultra-performance liquid chromatography-tandem mass spectrometry. *Anal Methods* 2013;5:1155.

Received August 18, 2020. Accepted April 6, 2021.

Correspondence

Address correspondence to: Deborah Stroka, PhD, Department for BioMedical Research, University of Bern, Murtenstrasse 35, 3008 Bern, Switzerland. e-mail: deborah.stroka@dbmr.unibe.ch; fax: (41)31 382 45 08.

Acknowledgements

The authors thank the Next Generation Sequencing platform at the University of Bern for their technical assistance with the RNAseq experiments. The authors also would like to acknowledge Carlos Wotzkow and Dr Fabian Blank from the Live Cell Imaging facility in Bern for their assistance with microscopy. Light and electron microscopy were performed on devices supported by the Microscopy Imaging Center of the University of Bern. The authors thank Donna Emge for creation of the Oil-Red-O staining protocol. The authors also thank the animal caretakers Anna Maria Jablonkowska and Nicole Ligocka for their support with animal housing and monitoring. The authors thank Nicolas Melin for his critical reading of the manuscript.

CRediT Authorship Contributions

Felix Alexander Baier, PhD (Conceptualization: Supporting; Data curation: Lead; Formal analysis: Lead; Investigation: Equal; Methodology: Lead; Visualization: Lead; Writing – original draft: Equal; Writing – review & editing: Equal)

Daniel Sánchez-Taltavull, PhD (Formal analysis: Supporting; Methodology: Supporting; Software: Supporting; Validation: Supporting; Visualization: Supporting; Writing – review & editing: Supporting)

Tural Yarahmadov, PhD (Formal analysis: Supporting; Methodology: Supporting; Software: Supporting; Validation: Supporting; Visualization: Supporting; Writing – review & editing: Supporting)

Cristina Gómez Castellà, PhD (Formal analysis: Supporting; Methodology: Supporting; Resources: Supporting; Validation: Supporting)

Fadi Jebbawi, PhD (Formal analysis: Supporting; Methodology: Supporting; Resources: Supporting; Software: Supporting; Validation: Supporting)

Adrian Keogh, PhD (Methodology: Supporting; Resources: Supporting; Validation: Supporting; Writing – review & editing: Supporting)

Riccardo Tombolini, - (Methodology: Supporting; Resources: Supporting)

Adolfo Odriozola, - (Methodology: Supporting; Resources: Supporting)

Mariana Castro Dias, PhD (Resources: Supporting)

Urban Deutsch, PhD (Resources: Supporting; Writing – review & editing: Supporting)

Mikio Furuse, Prof (Resources: Supporting)

Britta Engelhardt, Prof (Funding acquisition: Supporting; Resources: Supporting; Writing – review & editing: Supporting)

Benoît Zuber, Prof (Funding acquisition: Supporting; Resources: Supporting; Writing – review & editing: Supporting)

Alex Odermatt, Prof (Funding acquisition: Supporting; Resources: Supporting; Writing – review & editing: Supporting)

Daniel Candinas, Prof (Funding acquisition: Supporting)

Deborah Stroka, Prof (Conceptualization: Lead; Formal analysis: Supporting; Funding acquisition: Lead; Investigation: Equal; Project administration: Lead; Resources: Supporting; Supervision: Lead; Validation: Lead; Writing – original draft: Equal; Writing – review & editing: Equal)

Conflicts of interest

The authors disclose no conflicts.

Funding

Supported by Swiss National Science Foundation grant numbers 173157 (D.S.), 189080 (B.E.), 179520 (B.Z.), and 179400 (A.I.O.). The European Union Seventh Framework Program FP7 under grant agreements 241861 (Blood-brain barrier JUnctionS as Targets for paracellular drug delivery to the BRAIN) and 607962 (Neuroinflammation).